

1 **Spatiotemporal analysis of glioma heterogeneity reveals Col1A1 as an actionable** 2 **target to disrupt tumor mesenchymal differentiation, invasion and malignancy**

3
4 Andrea Comba^{1,2,3}, Syed M. Faisal^{1,2,3}, Patrick J. Dunn^{1,2,3}, Anna E. Argento^{1,2}, Todd C. Hollon¹, Wajd
5 N. Al-Holou¹, Maria Luisa Varela^{1,2,3}, Daniel B. Zmler^{1,2,3}, Gunnar L Quass⁷, Pierre F. Apostolides^{7,8},
6 Christine E. Brown⁹, Phillip E. Kish^{1,5}, Alon Kahana⁵, Celina G. Kleer^{3,6}, Sebastien Motsch⁴, Maria G
7 Castro^{1,2,3}, Pedro R. Lowenstein^{1,2,3,10}, *

8 ¹Dept. of Neurosurgery, University of Michigan Medical School, Ann Arbor, 48109, MI, USA

9 ²Dept. of Cell and Developmental Biology, University of Michigan Medical School, Ann Arbor, 48109 MI, USA

10 ³Rogel Cancer Center, University of Michigan Medical School, Ann Arbor, 48109, MI, USA

11 ⁴School of Mathematical and Statistical Sciences, Arizona State University, Tempe, AZ, USA

12 ⁵Ophthalmology & Visual Science, University of Michigan Medical School, Ann Arbor, 48109 MI, USA

13 ⁶Dept. of Pathology, University of Michigan Medical School, Ann Arbor, MI 48109, USA

14 ⁷Kresge Hearing Research Institute, Department of Otolaryngology-Head & Neck Surgery, University of
15 Michigan Medical School, Ann Arbor, MI 48109, USA

16 ⁸Dept. of Molecular & Integrative Physiology, University of Michigan Medical School, Ann Arbor, MI 48109,
17 USA.

18 ⁹Departments of Hematology & Hematopoietic Cell Transplantation and Immuno-Oncology, City of Hope,
19 Duarte, CA, USA.

20 ¹⁰ Dept. of Biomedical Engineering, University of Michigan, Ann Arbor, MI 48109,

21 *Correspondence to: pedrol@umich.edu

22

23 **ABSTRACT**

24 Intra-tumoral heterogeneity and diffuse infiltration are hallmarks of glioblastoma that challenge
25 treatment efficacy. However, the mechanisms that set up both tumor heterogeneity and invasion
26 remain poorly understood. Herein, we present a comprehensive spatiotemporal study that aligns
27 distinctive intra-tumoral histopathological structures, oncostreams, with dynamic properties and a
28 unique, actionable, spatial transcriptomic signature. Oncostreams are dynamic multicellular
29 fascicles of spindle-like and aligned cells with mesenchymal properties, **detected using *ex vivo***
30 **explants and *in vivo* intravital imaging**. Their density correlates with tumor aggressiveness in
31 genetically engineered mouse glioma models, and high grade human gliomas. Oncostreams
32 facilitate the intra-tumoral distribution of tumoral and non-tumoral cells, and the invasion of the
33 normal brain. These fascicles are defined by a specific molecular signature that regulates their
34 organization and function. Oncostreams structure and function depend on overexpression of
35 COL1A1. COL1A1 is a central gene in the dynamic organization of glioma mesenchymal
36 transformation, and a powerful regulator of glioma malignant behavior. Inhibition of COL1A1
37 eliminated oncostreams, reprogramed the malignant histopathological phenotype, reduced
38 expression of the mesenchymal associated genes, **induced changes in the tumor microenvironment**
39 and prolonged animal survival. Oncostreams represent a novel pathological marker of potential
40 value for diagnosis, prognosis, and treatment.

41

42 INTRODUCTION

43 High grade gliomas (HGG) are the most prevalent and malignant brain tumors. They grow rapidly,
44 invade surrounding normal brain, and recur within 12 months. Median survival is 18-20 months, in
45 spite of current standard of care^{1,2}. Despite some notable successful outcomes from the large cancer
46 sequencing programs, which identified driver genes in a number of cancers, effective
47 therapeutically actionable breakthroughs have not yet been identified in HGG³⁻⁷.

48 HGG are highly heterogeneous at the histological, cellular, and molecular level. Heterogeneity of
49 HGG is illustrated in addition by characteristic pathological structures such as pseudopalisades,
50 microvascular proliferation, and areas of hypoxia and necrosis^{2,8}. The molecular characterization of
51 glioma heterogeneity identified three main molecular signatures: proneural, mesenchymal, and
52 classical^{4,9}. However, later studies demonstrated that all three transcriptomic signatures are
53 expressed within individual tumors^{5,10,11}. Rather than outright glioma subtypes, the consensus
54 proposes that individual tumors are enriched in particular molecular subtypes. Thus, studies have
55 correlated histological features with genetic alterations and transcriptional expression patterns. For
56 example, highly aggressive histological features such as hypoxic, perinecrotic and microvascular
57 proliferative zones have been associated with the mesenchymal molecular signature and worse
58 prognosis⁸. However, the molecular classification has only minor clinical impact. Thus, alternative
59 classification schemes using a pathway-based classification are currently being considered¹². How
60 these new classifications will deal with tumor heterogeneity remains to be explored. **Moreover,**
61 **different microenvironmental, metabolic, and therapeutic factors drive transitions of the GBM**
62 **transcriptomic signature, particularly transitions to mesenchymal states. It is important to note that**
63 **glioblastoma plasticity explains the high degree of tumor heterogeneity and prompts the selection**
64 **of new clones at recurrence or therapy resistance¹³⁻¹⁶. It has been established that intra-tumoral**
65 **heterogeneity is represented by four main cellular states, the progenitor, astrocyte,**
66 **oligodendrocyte, and mesenchymal like-state, which represent tumor plasticity and are affected by**
67 **the tumor microenvironment¹⁵.**

68 Tumoral mesenchymal transformation is a hallmark of gliomas^{13,17,18}. A mesenchymal phenotype is
69 defined by cells with spindle-like, fibroblast-like morphology associated with alterations in their
70 dynamic cellular organization leading to an increase in cell migration and invasion^{19,20}. The
71 mesenchymal phenotype is controlled by particular transcription factors and downstream genes
72 related to the extracellular matrix (ECM), cell adhesion, migration, and tumor angiogenesis^{18,21,22}.

73 However, the cellular and molecular mechanisms that regulate mesenchymal transformation in
74 gliomas, especially concerning the mesenchymal features of invasive cells, has remained elusive.
75 Integrating morphological features, spatially resolved transcriptomics, and cellular dynamics
76 resulting from mesenchymal transformation, growth, and invasion are thus of great relevance to
77 our understanding of glioma progression^{13,20}.

78 Cell migration is essential to continued cancer growth and invasion. Morphological and biochemical
79 changes that occur during mesenchymal transformation allow glioma cells to move throughout the
80 tumor microenvironment and invade the adjacent normal brain. Tumor cells also migrate along
81 blood vessels, white matter tracks, and the subpial surface. Within the tumor microenvironment,
82 aligned extracellular matrix fibers help guide the movement of highly motile mesenchymal-like
83 cancer cells²³⁻²⁵.

84 Our study reveals that malignant gliomas, both high grade human gliomas and mouse glioma
85 models, display regular distinctive anatomical multicellular fascicles of aligned and elongated,
86 spindle-like cell. We suggest they are areas of mesenchymal transformation. For the sake of
87 simplicity in their description throughout the manuscript, we have named these areas
88 ‘oncostreams’.

89 Using time lapse laser scanning confocal imaging *ex vivo*, and multiphoton microscopy *in vivo* of high
90 grade glioma explants we demonstrated that oncostreams are organized collective dynamic
91 structures; they are present at the tumor core and at areas of tumor invasion of the normal brain.
92 Collective motion is a form of collective behavior where individual units’ (cells) movement is
93 regulated by local intercellular interactions (i.e., attraction/repulsion) resulting in large scale
94 coordinated cellular migration²⁶⁻³⁰. Collective motion plays an essential role in embryogenesis and
95 wound healing^{27,31-33}. Emergent organized collective motion patterns could help explain so far
96 poorly understood tumoral behaviors such as invasion, metastasis, and especially recurrence^{27,31}.

97 Studies of tumor motility have concentrated on the behavior of glioma cells at the tumor invasive
98 border^{27,34,35}. Potential motility at the glioma core has not been studied in much detail so far. This
99 study challenges the conventional belief that cells in the central core are non-motile and indicate
100 that the glioma core displays collective migratory patterns. This would suggest that the capacity of
101 gliomas to invade and grow, results from phenomena occurring at the tumor invasive border, and
102 from the overall capacity of gliomas to organize collective motion throughout the tumor mass, from
103 the tumor core to the tumor invasive border.

104 To study the molecular mechanisms underlying oncostream organization and function we used laser
105 capture microdissection (LCM) followed by RNA-sequencing and bioinformatics analysis. We
106 discovered that oncostreams are defined by a mesenchymal transformation signature enriched in
107 extracellular matrix related proteins, and which suggest that Collagen1A1 (COL1A1) is a key
108 determinant of oncostream organization. Inhibition of COL1A1 within glioma cells lead to
109 oncostream loss and reshaping of the highly aggressive phenotype of HGG. These data indicate that
110 COL1A1 is likely to constitute the tumor microenvironment scaffold, and to serve to organize areas
111 of collective motion in gliomas.

112 COL1A1 has been shown previously to be a major component of the extracellular matrix in different
113 cancers, including glioma, and has been reported to promote tumor growth and invasion^{36,37}.
114 Alternatively, some data suggest that collagen fibers could be passive barriers to resist tumor cell
115 infiltration or provide biophysical and biochemical support for cell migration. Some studies reported
116 that density of COL1A1 inversely correlates with glioma patient's prognosis. However, other studies
117 showed that either increased or decreased deposition of collagen could be associated with
118 increased tumor malignancy³⁸⁻⁴⁰. Therefore, it is important to further determine the role of COL1A1
119 in glioma invasion and continued growth.

120 This study provides a comprehensive study of the histological, morphological, and dynamic
121 properties of glioma tumors. In addition, we uncover a novel characterization of the molecular
122 mechanisms that define intra-tumoral mesenchymal transformation in gliomas and discuss their
123 therapeutic implications. Oncostreams are anatomically and molecularly distinctive, regulate glioma
124 growth and invasion, display collective motion, and are regulated by the extracellular matrix,
125 specially by COL1A1. Inhibiting COL1A1 within glioma cells is a potential therapeutic strategy to
126 mitigate glioma mesenchymal transformation, intra-tumoral heterogeneity, and thus, reduce
127 deadly glioma invasion and continued growth.

128

129

130

131

132

133

134

135 RESULTS

136 Intra-tumoral multicellular fascicles of elongated and aligned cells in gliomas: oncostreams

137 High grade gliomas (HGG) are characterized by anatomical, cellular and molecular heterogeneity
138 which determines, in part, tumor aggressiveness and reduces treatment efficacy^{5,7,11}.
139 Histopathological analysis of mouse and human gliomas revealed the presence of frequent distinct
140 multicellular fascicles of elongated (spindle-like) and aligned cells (\approx 5-30 cells wide) distributed
141 throughout the tumors. These structures resemble areas of mesenchymal transformation which we
142 describe as “oncostreams” (Fig. 1A-B).

143 To study the presence and morphological characterization of oncostreams, we examined
144 histological sections from various mouse glioma models as well as human glioma specimens (Fig. 1
145 A-B). We determined the existence of oncostreams in genetically engineered mouse models
146 (GEMM) of glioma including NPA (Nras, shP53, shATRx) and NPD (Nras, shP53, PDGF β) and other
147 implantable models (GL26) (Fig. 1A and Supplementary Fig. 1A-B). Moreover, human glioma
148 samples from primary resections and a xenograft glioma model, SJGBM2, established the presence
149 of these multicellular structures in human tissue (Fig. 1B and Supplementary Fig. 1C).
150 Morphological analysis determined that cells within histological areas corresponding to
151 oncostreams have an aspect ratio of 2.63 ± 0.19 (elongated or spindle-like cells) compared to the
152 surrounding tissue where cells have an aspect ratio of 1.37 ± 0.12 (round cells), both in mouse and
153 human gliomas as shown in Fig. 1C and Supplementary Fig. 1D. We also determined that elongated
154 cells within oncostreams are nematically aligned with each other, whereas outside of oncostreams,
155 cell orientations are not aligned (Fig. 1D and Supplementary Fig. 1E).

156 To gain insight into the cellular features of oncostreams we asked if they are homogeneous or
157 heterogeneous multicellular structures. We observed that in GEMM of gliomas, oncostreams are
158 formed by GFP+ tumor cells, and are enriched in other tumor microenvironment cells such as
159 ACTA2+ mesenchymal cells, Iba1+ and CD68+ tumor associated microglia/macrophages cells,
160 Nestin+ cells and GFAP+ glial derived cells (Fig. 1, E-G, and Supplementary Fig. 2 A-D). The
161 quantification of mesenchymal cells (ACTA2+), and tumor associated microglia/macrophages (TAM)
162 cells (CD68+ and Iba1+) showed a significant enrichment of these populations within oncostreams
163 compared to the surrounding areas (Fig. 1E-G). Moreover, non-tumoral cells within oncostreams
164 were positively aligned along the main axes of oncostreams, and with tumor cells in mouse gliomas

165 **(Fig. 1H)**. This suggests that oncostreams are mesenchymal-like structures which interact with TAM
166 and mesenchymal cells.

167 To test if oncostreams form along existing brain structures, we evaluated their co-localization with
168 white matter tracts. Although, occasional positive immune-reactivity (Neurofilament-L) was present
169 within some areas of the tumors, oncostream fascicles were not preferentially organized along brain
170 axonal pathways (**Supplementary Fig. 1F**). These data indicate that oncostreams are fascicles of
171 spindle-like aligned cells within glioma tumors, which contain tumor and non-tumor cells.

172

173 **Oncostream density positively correlates with tumor aggressiveness and poor prognosis in mouse
174 and human gliomas**

175 Oncostreams are unique histological features that contribute to intra-tumoral heterogeneity
176 suggesting a potential role in glioma progression and malignancy. To understand whether the
177 presence of oncostreams correlates with tumor aggressiveness and clinical outcomes, we generated
178 genetically engineered tumors of different malignant behaviors using the Sleeping Beauty
179 Transposon system. These models reproduce the malignant histopathological features of gliomas
180 as demonstrated in previous studies⁴¹⁻⁴⁴. We induced tumors harboring two different genotypes:
181 (1) Activation of RTK/RAS/PI3K pathway, in combination with p53 and ATRX downregulation (**NPA**),
182 and, (2) RTK/RAS/PI3K activation, p53 downregulation, ATRX downregulation, and mutant IDH1-
183 R132 expression (**NPAI**) (**Fig. 2A**). IDH1-wild-type tumors (**NPA**) display a highly malignant
184 phenotype and worse survival prognosis (Median survival (MS): 70 days), compared with tumors
185 harboring the IDH1-R132R mutation, **NPAI**, (MS: 213 days) (**Fig. 2B**). This outcome reproduces
186 human disease, as patients with IDH1-mutant tumors also have prolonged median survival^{1,44,45}.
187 Tumor histopathological analysis showed a positive correlation between the density of oncostreams
188 and tumor malignancy (**Fig. 2C- D**). NPA (IDH1-WT) tumors exhibited larger areas of oncostreams
189 within a highly infiltrative and heterogeneous glioma characterized by abundant necrosis,
190 microvascular proliferation, pseudopalisades and cellular heterogeneity as described before^{43,44}.
191 Conversely, NPAI (IDH1-Mut) tumors display a very low density of oncostreams and a homogenous
192 histology mainly comprised of round cells, low amounts of necrosis, no microvascular proliferation,
193 absence of pseudopalisades and less invasive borders (**Fig. 2C and Supplementary Fig. 5**).

194 Further, to objectively identify and quantify tumor areas covered by oncostreams, we trained a fully
195 convolutional neural network (fCNN) (**Supplementary Fig. 3 and 4A**). Our deep learning analysis

196 found that oncostreams occupied $15.28 \pm 6.10\%$ of the area in NPA tumors compared with only 1.18
197 $\pm 0.81\%$ in NPAI tumors (**Fig. 2C and D, and Fig. Supplementary 5A and B**). Cellular alignment
198 analysis validated the presence or absence of oncostreams (**Fig. 2E**).

199 To determine whether oncostreams are linked to glioma aggressiveness in human patients, we
200 evaluated a large cohort of TCGA glioma diagnostic tissue slides from the Genomic Data Commons
201 Portal of the National Cancer Institute. We visually examined 100 TCGA-glioblastoma multiforme
202 tissue sections (WHO Grade IV) and 120 TCGA-low grade glioma tissues (WHO Grade II and III) using
203 the portal's slide image viewer (**Supplementary Table 1**). Oncostreams were present in 47% of
204 TCGA-GBM grade IV tumors tissue, in 8.6 % of TCGA-LGG grade III, and were absent from TCGA-LGG
205 grade II (**Fig. 3A-C and Supplementary Table 2**), consistent with tumor aggressiveness
206 (<http://gliovis.bioinfo.cnio.es>)⁴⁶. We then determined the presence of oncostreams across known
207 molecular subtypes of HHG (Grade IV)⁴. We found oncostream fascicles in 59.4% of Mesenchymal
208 (MES), 53.6% of Classical (CL) subtypes and only 26.7% of Proneural (PN) (**Fig. Supplementary 6A**).
209 Finally, we evaluated oncostreams presence related to IDH status and 1p 19q co-deletion in LGG
210 (Grade III). Oncostreams were present in 16.6% of IDH-WT subtype, 5% of IDHmut-non-codel and
211 absent from IDHmut-codel subtype (**Fig. Supplementary 6B**). These analyses suggest that
212 oncostream presence is higher in Mesenchymal and Classical subtypes and correlates with IDH-WT
213 status, and thus with a poor prognosis.

214 To validate the histological identification, we examined H&E images using our deep learning
215 algorithm (**Fig. Supplementary 4B**). We observed a strong concordance (>84%) between machine
216 learning and the manual histological identification of oncostreams (**Table Supplementary 3**).
217 Oncostream presence and their segmentation by deep learning is illustrated in **Fig. 3C and**
218 **Supplementary Fig. 7 and 8**. Additionally, alignment analysis of glioma cells confirmed the existence
219 of fascicles of elongated, mesenchymal-like cells in human gliomas (**Fig. 3D**). Thus, our deep learning
220 algorithm validates our histological identification of oncostreams and confirms that the density of
221 oncostream fascicles positively correlates with glioma aggressiveness.

222 The analysis of cellular heterogeneity showed that non-tumoral cells such as Iba1+
223 macrophages/microglia and GFAP+ glial derived cells were positively aligned within oncostreams
224 tumoral cells (SOX+) in human HGG (**Fig. 3E**). Conversely, we detected that low grade gliomas (LGG)
225 exhibited homogenous round cells, GFAP+ and Iba1+ cells throughout the tumor with no defined
226 orientation or alignment (**Fig. 3F**).

227

228 **Oncostreams are defined by a distinctive spatial transcriptome signature**

229 To determine whether oncostreams fascicles are characterized by a specific gene expression profile,
230 we performed a spatially-resolved transcriptomic analysis using laser capture microdissection (LCM)
231 coupled to RNA sequencing (RNA-Seq). Oncostreams were dissected according to their
232 morphological characteristics defined above. Surrounding areas of homogenous rounded cells were
233 selected as non-oncostreams areas (control) (**Fig. 4A**). RNA-Seq analysis detected a set of 43
234 differentially expressed (DE) genes; 16 genes were upregulated and 27 downregulated within
235 oncostreams (**Fig. 4 B-C and Table Supplementary 4**).

236 Functional enrichment analysis of DE genes, performed using the I-PathwayGuide platform (Advaita
237 Corporation, MI, USA), showed that False Discovery Rate (FDR) corrected gene ontology (GOs)
238 terms were associated with migration and extracellular matrix biological process. GOs such as
239 “positive regulation of motility” “positive regulation of cell migration”, “collagen catabolic
240 processes” and “extracellular matrix organization” were the most over-represented biological
241 processes (**Fig. 4D and Table Supplementary 5**). The upregulated DE genes within the relevant GOs
242 include: COL1A1, MMP9, MMP10, ACTA2, ADAMTS2, CDH5, CYR61, PLP1 and those downregulated
243 were ENPP2, AKAP12, BDKRB1 (**Fig. 4E and Fig. Supplementary 9**). Significant DE genes shared by
244 related GOs are shown in **Supplementary Fig. 9**. These data indicate that oncostreams can be
245 identified by a specific gene expression set and suggest a distinct role for oncostreams as intra-
246 tumoral mesenchymal-like migratory assemblies within glioma tumors.

247

248 **COL1A1 contributes to oncostream organization in high-grade gliomas**

249 Histopathologically, oncostreams are spindle-like multicellular fascicles with a defined DE gene
250 expression signature enriched in mesenchymal genes. The GO ontology analyses suggests a central
251 role of collagen catabolic process and extracellular matrix organization in oncostreams function. To
252 understand the molecular mechanisms that regulate oncostream organization and function, we
253 identified critical genes using network analysis. Network interactions revealed that COL1A1 is a hub
254 gene, one of the most highly connected nodes, representing a potential regulator of the network’s
255 signaling pathways and biological functions (**Fig 5A and Fig. Supplementary 10A**). We found that
256 the most relevant COL1A1 related pathways include: Focal Adhesion, Extracellular Matrix

257 Organization and Integrin Signaling pathways (**Fig. Supplementary 10B-C and Table Supplementary**
258 **7 and 8**).

259 To analyze the role of COL1A1 in oncostream organization, we analyzed COL1A1 expression by
260 immunofluorescence analysis. The COL1A1 gene encodes for the alpha-1 chain of type I collagen
261 fibers. We observed that collagen fibers were aligned within oncostreams and overexpressed in
262 more aggressive NPA (IDH1-WT) gliomas compared with NPAI (IDH1-Mut) tumors. COL1A1
263 expression was significantly lower and only found surrounding blood vessels in NPAI (IDH-Mut)
264 tumors (**Fig. 5B-C**). Correspondingly, human GBM glioma tumors (IDH1-WT) with high oncostream
265 densities showed prominent alignment of collagen fibers along these fascicles and higher COL1A1
266 expression compared to LGG (IDH1-Mut) (**Fig. 5D and E**).

267 Moreover, TCGA-glioma data indicate that COL1A1 has differentially higher expression in GBM
268 histological Grade IV. LGG IDH-WT tumors display higher expression of COL1A1 than IDH1-Mutant.
269 Within the GBM molecular subtype classification^{4,9}, the Mesenchymal group shows higher
270 expression of COL1A1 than the Proneural and Classical groups (**Fig. Supplementary 11A**); the
271 COL1A1 gene is clearly associated with the mesenchymal subtype. Analysis of patient survival
272 related to COL1A1 expression showed that mesenchymal GBM subtype displayed a significantly
273 shorter survival (MS: 10.4 months) for COL1A1 high tumors, compared to COL1A1 low (MS: 17.9
274 months) tumors. Classical and Proneural subtypes did not show survival differences associated to
275 COL1A1 expression (**Fig. Supplementary 11B**). Thus, oncostreams represent intra-tumoral
276 mesenchymal-like structures organized along collagen fibers.

277

278 **COL1A1 depletion leads to oncostream loss, tumor microenvironment (TME) remodeling and**
279 **increases in median survival**

280 To evaluate the functional role of COL1A1 in oncostream formation we generated a COL1A1-
281 deficient genetically engineered mouse glioma model. We generated COL1A1 wildtype, and COL1A1
282 knock-down tumors with different genetic backgrounds (**Fig Supplementary 12A-C**). COL1A1
283 downregulation increased median survival (MS) (**Fig. 5F and G**). The knockdown of COL1A1 in NPA
284 tumors (NPAs^hCOL1A1) increased survival to MS: 123 days, compared to NPA control tumors (MS:
285 68 days) (**Fig. 5F**). Similarly, COL1A1 knockdown in NPD tumors harboring PDGF β ligand upregulation
286 (NPD^{sh}COL1A1), also exhibited an increased median survival (MS: 98 days) compared to the NPD
287 controls (MS: 74 days) (**Fig. 5G**).

288 To further analyze the effects of COL1A1 downregulation, we evaluated the histopathological
289 features of glioma tumors, quantified oncostream density using deep learning analysis and
290 evaluated COL1A1 expression within glioma tissues (**Fig. 5 H-I**). We observed that NPA tumors with
291 COL1A1 downregulation showed a significant reduction of COL1A1 immunoreactivity within tumors;
292 it was only maintained in small areas surrounding blood vessels (**Fig. 5J-K**). COL1A1 inhibition led to
293 oncostream loss and reprogramming of the histopathological tumoral characteristics as evidenced
294 by homogenous round cell morphology, resembling low grade tumors (**Fig. 5J-K**). Downregulation
295 of COL1A1 in NPD tumors appeared less effective, with large areas of remaining COL1A1 (**Fig. 5H-I**).
296 Nonetheless, COL1A1 was downregulated within tumor cells and oncostream dismantling was
297 significant compared to NPD control. Some oncostream areas remained associated with blood
298 vessels which displayed significant amounts of COL1A1 (**Fig. 5J-K**).

299 We analyzed the effect of COL1A1 depletion on the intrinsic properties of tumoral cells. *In vitro*
300 studies showed that COL1A1-knockdown cells exhibited a significantly decreased cell proliferation
301 and cell migration compared to controls (**Supplementary Fig. 13 A-D**). Also, we observed that
302 intracranial implantation of COL1A1-knockdown cells resulted in decreased tumor growth and
303 progression when compared to controls (**Fig. Supplementary 13E**). *In vivo*, genetically engineered
304 COL1A1 knockdown tumors displayed decreased cell proliferation (PCNA+ cells) (**Fig. 6A-B**),
305 increased apoptosis via activation of Cleaved-Caspase 3, and downregulation of the anti-apoptotic
306 protein Survivin (**Supplementary Fig. 14A-C**).

307 Furthermore, to determine whether COL1A1 downregulation within glioma cells modifies the
308 glioma TME we analyzed changes in tumor associated macrophages (TAM), endothelial cells and
309 mesenchymal cells. We found that COL1A1 knockdown tumors exhibited a decreased recruitment
310 of CD68+ TAM (**Fig. 6C-D**), impaired CD31+ endothelial vascular proliferation (**Fig. 6E-F**) and
311 diminished ACTA2+ perivascular mesenchymal cells (**Fig. 6G-H**). Moreover, inhibition of COL1A1
312 within glioma cells led to downregulation of fibronectin expression, a mesenchymal associated
313 extracellular matrix protein (**Fig. Supplementary 14E-F**) that is associated with a more aggressive
314 phenotype.

315 These preclinical animal models knocked down the expression of COL1A1 from the earliest stages
316 of tumor development. Further, to evaluate the effects of the pharmacological degradation of
317 deposited collagen fibers in highly malignant tumors we analyzed explants of brain tumor sections
318 treated with collagenase. We observed that collagenase treatment decreased reticular fibers

319 (general collagen staining), reduced COL1A1 expression and disassemble fibers' alignment along
320 tumoral cells and caused oncostreams depletion in a dose dependent manner (**Fig. Supplementary**
321 **15A-D**). These data indicate that oncostream organization and functions are regulated by COL1A1.
322 COL1A1 knockdown within glioma cells decreased oncostream formation, reprogramed glioma
323 mesenchymal transformation and remodeled the glioma TME, thus increasing animal survival.
324 COL1A1 inhibition represents a novel approach for future translational development.

325

326 **Oncostreams' mesenchymal patterns reveal intra-tumoral collective motion in gliomas**

327 GO analysis indicates that biological processes such as positive regulation of motility/migration are
328 enriched within oncostream fascicles. Overexpression of extracellular matrix (ECM)-associated
329 proteins suggest a potential role of COL1A1 fibers in regulating oncostreams' motility. To study if
330 oncostreams represent migratory structures within glioma tumors, we established a physiologically
331 viable explant brain tumor slice model containing a high density of oncostreams (**Fig. 7A**). The
332 movement of glioma cells expressing green fluorescent protein (GFP), within the thickness of each
333 explant, was visualized using time-lapse confocal imaging and tracked using Fiji's plug-in Track-
334 Mate (**Fig. 7A-C**).

335 Migration analyses show complex glioma cell dynamics throughout the tumor core. The glioma
336 tumor core displays groups of cells (within particular zones) with similar nematic orientation and
337 displaying complex movement patterns (**Fig. 7D and Fig. Supplementary 16A**) and, which represent
338 collective motion^{27,29-31}. Angle velocity distribution indicated the existence of three patterns of
339 collective motility shown schematically in **Fig. 7D and F**: in 'Zone A' cells don't have a preferred
340 direction, in 'Zone B' cells move in opposite directions ($\sim 135^\circ$ and 315°), and in 'Zone C' all cells
341 move with a predominant preferred direction ($\sim 45^\circ$) (**Fig. 7D and F**). We named these patterns
342 '*swarm*' (Zone A), '*stream*' (Zone B), or '*flock*' (Zone C) (**Fig. 7G**). They were classified by likelihood
343 analysis: the distribution of the angle velocity is constant in a *swarm* (all angle velocity are equally
344 probable), bi-modal in a *stream* (cells are moving in equal but opposite directions), and uni-modal
345 in a *flock* (cells move in one direction) (**Fig. 7H**). These patterns were observed in all tumor slices
346 examined (**Fig. Supplementary 18, 19 and 20**). Average cell speeds differed among the three
347 patterns (**Fig. 7E, and Supplementary 18, 19 and 20**). In the tumor core, swarms moved faster and
348 without orientation, followed by directionally moving flocks and streams (**Fig. Supplementary 27**).
349 To determine which of these collective motion patterns match oncostream histological features, we

350 analyzed H&E sections corresponding to imaged organotypic slices (**Fig. Supplementary 16B**). Cells
351 within histological areas corresponding to *streams* and *flocks* have an aspect ratio of 2.2 and 2.7,
352 respectively, (spindle-like cells), while those within areas corresponding to *swarms* have an aspect
353 ratio of 1.2 (round cells) (**Fig. Supplementary 16C-D**). Moreover, elongated cells within *streams* and
354 *flocks* are nematically aligned with each other, whereas round cells within *swarms* are not (**Fig.**
355 **Supplementary 16E**). As predicted by our *in silico* model,⁴⁷ these results suggest that cell shape, or
356 eccentricity, is driving feature in the organization of collective motion patterns (**Fig. Supplementary**
357 **16F**). Therefore, taking into account cell shape and alignment, we define oncostreams as the
358 histological expression of collective motion patterns (*streams* and *flocks*). Notice that only the
359 dynamic analysis of collective motion can differentiate between *streams* and *flocks*. At the
360 histological level both appear as oncostreams.

361 In collective motion of flocks, interactions among individual cells are sufficient to propagate order
362 throughout a large population of starlings⁴⁸. To define if oncostream migration patterns recall
363 organized collective motion behavior, we analyzed the organization of the cells by performing local
364 pair-wise correlation analysis (relative position and pair directional correlation) by tumor zones (**Fig.**
365 **Supplementary 17A-C**). These analyses indicate the spatial correlation of location and alignment
366 between individual cells. We observed that within *swarms* cells are more separated, as neighbors
367 are located at 20-40 μm . *Streams* and *flocks* have higher cell density, and the nearest neighbors
368 are closer, at 20-30 μm (**Fig. Supplementary 17E and S18, S19, S20**). Pair-wise directional correlation
369 with nearby neighbors showed that cell movement is positively correlated in all patterns at
370 distances between 10-50 μm , with higher correlation left-to-right for *streams* (≈ 0.2), left-to-
371 right/front-to-back for *flocks* ($\approx 0.2-0.4$), and a lower correlation for *swarms* (≈ 0.1) (**Fig.**
372 **Supplementary 17F and S18, S19, S20**). We ascertained that tumor cells within oncostreams
373 migrate in a directional manner (“streams ($\uparrow\downarrow$)” and “flocks ($\uparrow\uparrow$)”), while non-oncostream cells
374 move randomly without directional alignment as “swarms”. Thus, our analyses strongly indicate
375 that within the tumor core of high grade glioma cells are dynamically heterogeneous and display
376 organized collective migratory behavior associated with tumor histological and genetic features.

377

378 **Oncostreams increase the intratumoral spread of tumoral and non-tumoral cells**

379 Pair-wise correlation analysis showed that oncostream glioma cells are collectively organized. To
380 test the underlying nature of collective oncostream motility, we analyzed adherent junction

381 markers. Tumors with oncostreams were negative for E-cadherin, whereas N-cadherin was strongly
382 expressed (**Fig. Supplementary 21A**), suggesting that these fascicles move in a manner akin to
383 collective migration of mesenchymal cells of the neural crest^{33,49}. Although, no difference in N-
384 cadherin were found within oncostreams and the surrounding areas, N-cadherin was elevated in
385 TCGA-GBM (Grade IV) tumors compared to TCGA-LGG (Grade III and II). High levels of N-cadherin
386 correlate with lower survival in HGG patients and mesenchymal transformation (**Fig.**
387 **Supplementary 21B-C**).

388 On the other hand, oncostream growth and motility is unlikely to be due to glioma proliferation.
389 BrdU staining showed no differences between oncostream and non-oncostream regions, and in the
390 oncostreams, the mitotic plane was always perpendicular to the main axis as expected (**Fig.**
391 **Supplementary 21D-E**). These results are also supported by the RNA-Seq data of dissected
392 oncostreams, where proliferation genes were not differentially expressed (**Fig. 4 A-C**).

393 Collective motion could affect the distribution of other cells within the tumor. Since oncostreams
394 are heterogeneous, we inquired about their pro-tumoral role by potentially spreading cells
395 throughout the tumor. We designed co-implantation experiments using human glioma stem cells
396 (MSP-12), and highly aggressive and oncostream-forming glioma cells (GL26) co-implanted into
397 immunosuppressed mice. Implantation of MSP-12 cells alone generated slow-growing tumors
398 (median survival of 6-8 months). At 21 days post-implantation, MSP-12 cells remained restricted to
399 the injection area with an average distance of $28.9 \pm 7.73 \mu\text{m}$ from the actual injection site.
400 Surprisingly, when MSP-12 cells were co-implanted with GL26-citrine cells, MSP-12 cells spread
401 throughout the tumor, moving along oncostreams to much longer distances ($83.7 \pm 23.74 \mu\text{m}$) from
402 the injection site (**Fig. 7I-K**). Cellular cytoplasmic processes from MSP-12 cells implanted alone
403 displayed a random distribution. However, in co-implanted tumors, such processes from MSP-12
404 cells are completely aligned with glioma GL26 cells within oncostreams (**Fig. 7K-L and Fig.**
405 **Supplementary 21F**). These results strongly suggest that oncostreams function as intra-tumoral
406 highways facilitating the rapid distribution of slow-moving glioma cells and/or non-tumor cells
407 throughout the tumor mass. These findings could help explain the dispersal and intratumoral
408 mixing of diverse clonal populations as demonstrated in previous studies, supporting an important
409 potential role of oncostreams in determining spatial cellular heterogeneity.

410

411 **Dynamic interactions at the tumor border: oncostreams foster glioma aggressiveness through**
412 **collective invasion of the normal brain parenchyma**

413 Furthermore, we asked whether oncostreams participate in glioma invasion. The analysis of
414 histological sections showed that multicellular fascicles of elongated and aligned cells are found
415 invading from the tumor border into the normal brain parenchyma (**Supplementary Fig. 22A**).
416 Formation of streams around blood vessels was also observed (**Supplementary Fig. 22A**). These
417 patterns of invasion are also detected using our deep learning methods (**Fig. Supplementary 22B**).
418 We then used our glioma explant model to analyze the invasion dynamics by time-lapse confocal
419 imaging at the tumor border (**Fig. 8A**). We implanted glioma NPA GFP+ cells into tdTomato (mT/mG)
420 mice so tumor borders could be delineated. We observed that glioma cells that extended from the
421 tumor border to the normal brain parenchyma used different dynamic patterns, moving as isolated
422 random cells and/or as collective migratory structures moving directionally, and resembled
423 oncostream structures similar to those in the tumor core (**Fig. 8B-G and Fig. Supplementary 23-25**).
424 To objectively distinguish between different dynamic patterns, we determined the angle velocity
425 distribution, and the likelihood that distributions corresponded to either a *stream*, a *flock*, or a
426 *swarm*. We found *streams* along the perivascular niche or invading brain parenchyma without
427 following any pre-existing brain structures, as well as cells invading as *flocks*, and *swarms* (**Fig. 8E-F,**
428 **and Fig. Supplementary 23-25 A, C and D**). Glioma cells moving along blood vessels or directly into
429 the brain as single cells is consistent with previous studies¹⁰. The correlation of position and velocity
430 supports the existence of invading collective motion structures in NPA tumors with high expression
431 of COL1A1 (**Fig. S22D-E**). We also determined the participation of collagen fibers in oncostreams
432 invasion. Immunofluorescence analysis on explant slices showed that collagen fibers are aligned
433 along multicellular fascicles of glioma cells invading the normal brain. These data show how collagen
434 fibers serve as scaffolds for collective tumoral cell invasion (**Fig. Supplementary S26**).
435 Our data indicate the existence of a complex framework of collective motion patterns at the glioma
436 border, that is consistent with previous descriptions³⁴. Although the patterns observed at the NPA
437 tumor border are similar to those of the tumor core, cell speed differed between the areas. Cells in
438 the tumor core displayed significantly lower average speeds (*stream*: 4.26; *flock*: 5.95, *swarm*: 6.27
439 $\mu\text{m/hr}$) compared to cells at the tumor border or those invading the normal parenchyma (*stream*:
440 7.95; *flock*: 7.55, *swarm*: 8.01 $\mu\text{m/hr}$) (**Fig. Supplementary 27A-B**).

441 Then, we asked whether the knockdown of COL1A1 in NPA gliomas affects changes in the patterns
442 of migration and invasion. Analysis of tumor cells (GFP+) at the tumor borders of GEMM of gliomas
443 comparing NPA and NPA-shCOL1A1 showed a difference in the apparent invasion patterns. The
444 analysis of tumor borders revealed an increase in the sinuosity of NPA tumors, a finding compatible
445 with NPA tumors exhibiting a higher proportion of collective invasion into the normal brain when
446 compared to NPA-shCOL1A1 tumors (Fig. 8G-I).

447 Moreover, the time lapse-confocal imaging and migration analysis of NPA-shCOL1A1 explants
448 showed that tumor cells invade the normal brain parenchyma as isolated cells (Supplementary Fig.
449 29-32). Velocity angle, velocity vector and the likelihood analysis indicated that the overall
450 distribution corresponded predominantly to *swarm* random patterns (Supplementary Fig. 29-32 D,
451 E, F). Further analysis of Relative Position Correlation and Pairwise correlation supports the
452 presence of low density of cells compatible with single cell invasion patterns in NPashCOL1A1
453 tumors with low expression of collagen (Supplementary Fig. S29-32 G,H).

454 We conclude that oncostreams (*streams* and *flocks*) are organized collective migratory structures
455 enriched in COL1A1 that participate in the dynamic organization of the tumor microenvironment
456 within the tumor core and at the tumor invasive border of high-grade gliomas, and facilitate invasion
457 into the normal brain, impacting the malignant behavior of gliomas. Depletion of collagen1A1
458 eliminates oncostreams and their associated functions.

459

460 **Intravital imaging of glioma reveals the existence of oncostreams collective motion patterns *in*** 461 ***vivo* and their contribution to invasion**

462 To analyze further, the previously described collective migration patterns of glioma cells we
463 performed high resolution time lapse intravital imaging using *in vivo* two photon microscopy. NPA
464 glioma cells were intracranially implanted in the brain of tdTomato (mT/mG) mice. To visualize the
465 migration of the cells we established a cranial window above the injection site. After 7-15 days of
466 tumor development, we acquired time lapse images of the tumor core and border with a time frame
467 of 5 minutes for 8-12 hours periods (Fig. 9A). The movement of GFP+ glioma cells was tracked using
468 Fiji's plug-in Track-Mate (Fig. 9B-C). The analysis of cell migration *in vivo* showed that the glioma
469 tumor core exhibits organized, nematically aligned cells moving collectively. Angle velocity
470 distribution analysis determined the existence of '*stream*' collective motion patterns as shown for
471 example in Fig. 9E, illustrating that nematically aligned cells are moving in opposite directions

472 (~ 65° and 250°). To corroborate the existence of ‘streams’ patterns we classified the movement by
473 likelihood analysis. For ‘streams’ the distribution of the angle velocity and velocity vectors showed
474 a bi-modal distribution (cells were moving in equal but opposite directions) same as we observed in
475 the explant models (**Fig. 9F and Supplementary Fig. S33A**). The analysis of cell speeds showed a
476 mean speed of 3.44 $\mu\text{m}/\text{hour}$ (**Fig. 9G**), in concordance with the speed found for streams in the
477 tumor core of the explant model (**Fig. 7E**).

478 To analyze the invasion of glioma cells, we focused the movement analysis at the tumor border (**Fig**
479 **9G-H**). We observed that cells at the tumor border displayed ‘stream’ collective dynamic patterns
480 (**Fig. 9I, Zone A**). Cells that spread from the tumor border to the normal brain (i.e., invasion) used
481 two different collective dynamic patterns: ‘streams’ (e.g., Zone B) and ‘flocks’ (e.g., Zone C) (**Fig. 9I**).
482 These motion patterns were determined by angle velocity distribution analysis, and likelihood
483 distribution analysis (**Fig. 9K-L and Supplementary Fig. S33 B**). Similar patterns were also observed
484 in further movies (**Fig. S33 C-H**). The collective motion patterns found *in vivo* resembled the
485 collective motions patterns described in the *ex vivo* explant model. Our results show that glioma
486 cells are organized in collective dynamic patterns at the tumor core and the tumor invasive border,
487 in tumor explants and in *in vivo* intravital models of gliomas, analyzed by two photon microscopy.

488

489 DISCUSSION

490 Mesenchymal transformation is a hallmark of tumor heterogeneity that is associated with a more
491 aggressive phenotype and therapeutic resistance^{13,18,21}. Mesenchymal transformation involves
492 fibroblast-like morphological changes associated with active migration and gain of expression of
493 mesenchymal genes as previously described^{21,22}.

494 Herein we present a comprehensive study that defines the morphological, cellular, dynamic, and
495 molecular properties of multicellular mesenchymal-like structures within gliomas. These structures
496 are fascicles of aligned spindle-like cells found throughout the tumors and represent areas of
497 mesenchymal transformation. We interpret these structures to be the histological expression of
498 areas of collective motion of glioma cells. For the sake of simplicity, we have referred to these areas
499 of mesenchymal transformation as oncostreams.

500 Oncostreams are areas of mesenchymal transformation and are identified histologically as fascicles
501 of aligned and elongated cells. When examined dynamically, we found that tumor cells move by
502 collective motion within the tumor core and at the invading border. The capacity to identify areas

503 of collective motion in histological sections has allowed us to characterize the molecular
504 organization of such dynamic structures. We thus describe the overall molecular mechanisms that
505 govern the organization and function of these structures and demonstrate the causal role of
506 individual mediators. Surprisingly, we discovered that COL1A1 is central to the structural and
507 dynamic characteristics of oncostreams. Indeed, the loss of COL1A1 expression from tumor cells
508 disrupts the structural and functional characteristics of oncostreams, resulting in a complete loss of
509 mesenchymal areas within gliomas and a reduction in glioma malignant behavior (**Fig. 10**).

510 The analysis of the gene ontologies over-represented within oncostreams indicates that
511 oncostreams denote areas enriched for “positive regulation of cell migration”, and in mesenchymal
512 related genes. Interestingly, COL1A1 appeared as a central hub of oncostream organization and
513 mesenchymal transformation. We postulate that oncostreams are the histopathological expression
514 of patterns of collective motion (i.e., streams and flocks) in high grade glioma tumors. Different
515 strategies of cell migration encountered in our gliomas are reminiscent of migratory characteristics
516 observed during embryonic development^{31,32,49}. In developmental biology, collective motion is
517 represented by cells moving together in clusters, sheets, streams, or other multicellular
518 arrangements^{28,31,32}.

519 Our studies of oncostream dynamics at the tumor core are compatible with the results of Ralitzta et
520 al⁵⁰. This group studied *ex-vivo* explant slices of spontaneous intestinal carcinoma, and showed that
521 cells within the tumor core were highly dynamic and display directionally correlated cell motion⁵⁰,
522 similar to our results described herein. Recent *in silico* based mathematical modelling of glioma cell
523 dynamics by our group, showed that only elongated cells, but not spherical cells, are able to form
524 organized aligned cellular structures in a cell-density dependent manner⁴⁷. Our modeling studies
525 strongly support our *in-vivo* and *ex-vivo* data described in this manuscript.

526 Moreover, it has been described that increased matrix cross-linking, enzymatic remodeling and
527 parallel orientation of matrix collagen fibers stiffens tissue, modifies cell morphology and promotes
528 cell migration and invasion^{36,38,39,51,52}. Our results support the proposal that oncostreams serve as
529 highways to spread tumor, and non-tumor cells, throughout the tumor. **Indeed, oncostream**
530 **fascicles contain higher amounts of macrophages/microglia and mesenchymal cells.** Dispersal of
531 tumor and non-tumoral cells throughout the tumors could help explain the mixing of different clonal
532 populations seen in molecular studies of high-grade gliomas¹⁰.

533 This study contributes to explaining how a particular feature of intratumoral heterogeneity, namely
534 mesenchymal transformation, affects HGG progression. Our data indicate that the density of
535 oncostreams plays a potential role in overall glioma malignant behavior in mouse and human
536 gliomas.

537 Spatially resolved transcriptional analysis using laser capture microdissection provided novel
538 insights into the molecular mechanisms that regulate oncostream functions. Oncostreams were
539 defined by a unique transcriptomic signature that matched our immunohistochemical studies.
540 COL1A1 overexpression within oncostreams was complemented with the overexpression of
541 extracellular matrix proteins such as MMP9, MMP10, ADAMTS2, which are known to remodel and
542 participate in the reorganization of collagen fibers. Oncostream fascicles were correspondingly
543 enriched in COL1A1 when assessed by immunohistochemistry.

544 Within the extracellular matrix, collagen fibers constitute a scaffold for the organization of the
545 tumor microenvironment and thus promote tumor infiltration and invasion. While collagen was
546 previously thought to be a passive barrier that could reduce tumor invasion, it has now been shown
547 that collagen fibers can serve as mechanical and biochemical tracks that facilitate cellular migration
548 and tumor progression^{36-38,53}. Previously, multi-cancer computational analysis found that within a
549 mesenchymal transformation signature in different cancers including gliomas, COL1A1 was one of
550 the top differentially expressed genes^{18,22,54}. COL1A1 is overexpressed in high grade malignant
551 gliomas and its expression levels are inversely correlated with patient survival⁵⁵ as indicated in
552 <https://www.cancer.gov/tcga>. In our mouse glioma models and in human gliomas, tumors with
553 higher density of oncostreams also express higher levels of COL1A1. COL1A1 is a consistently
554 differentially expressed gene in the glioma mesenchymal signature identified in malignant gliomas
555 and in glioma stem cells as described in previous studies^{4,9,56}. Overall, our data are in agreement
556 with a recent study by Puchalski *et al.*, which assigned genetic and transcriptional information to
557 the most common morphological hallmarks of a glioma, emphasizing the importance of integrative
558 histo-molecular studies⁸.

559 Surprisingly, our data indicate a remarkable plasticity of the mesenchymal phenotype in gliomas,
560 **similar to other studies**^{13,15}. Genetic inhibition of COL1A1 within glioma cells depleted COL1A1 from
561 tumors, eliminated oncostream structures, reduced the glioma malignant phenotype, and
562 prolonged animal survival. Our findings are comparable with results from various studies that
563 investigated the *in-vitro* and *in-vivo* consequences of collagen depletion, inhibition of collagen cross-

564 linking or collagen synthesis inhibition on normalizing tumor ECM. In these studies, inhibition of
565 collagen led to changes in the ECM which improved drug penetration, efficacy, as well as tumor
566 access of therapeutic nano-particles or gene based therapies⁵⁷⁻⁶¹. In addition, COL1A1 inhibition
567 within glioma cells induced cell intrinsic and extrinsic changes in the TME. COL1A1 inhibition not
568 only inhibits tumor cell proliferation and migration but also decreased the infiltration of
569 microglia/macrophages, endothelial cells proliferation, and perivascular mesenchymal-like cells. As
570 previously shown by other studies, glioblastomas exhibit a complex interaction between tumoral
571 and non-tumoral cells including macrophages, immune cells, endothelial cells that influence tumor
572 growth, transformation, and invasion affecting the response to treatment^{9,13,62}. However, a major
573 remodeling of the tumor mesenchymal phenotype in response to inhibition of COL1A1 has not been
574 described earlier.

575 Moreover, we found that multicellular oncostream fascicles are detected in both *ex vivo* and *in*
576 *vivo* glioma models, and that oncostreams facilitate tumor cell invasion thereby increasing glioma
577 aggressiveness. Our findings strongly support the importance of collective motility of cancer cells in
578 the progression of tumor growth and invasion of normal brain parenchyma, as evidenced by earlier
579 studies of normal and pathological conditions^{27,34,35,63-67}.

580 In summary, our observations suggest that oncostreams are morphologically and molecularly
581 distinct structures that represent areas of collective motion that contribute to tumor growth and
582 invasion. These malignant dynamic structures overexpress COL1A1. COL1A1 knockdown eliminates
583 oncostreams, reduces the mesenchymal phenotype, modifies the TME and delays tumor
584 progression. Our findings open new paths to understanding tumor mesenchymal transformation
585 and its therapeutic treatment. We propose that depletion of COL1A1 within oncostreams is a
586 promising approach to reprogram mesenchymal transformation in glioma tumor as a novel
587 therapeutic approach, and thus reduce the glioma malignant phenotype.

588

589 **METHODS**

590 **Glioma cell lines and culture conditions:**

591 Mouse glioma cells (NPA, NPD, NPAsCol1A1, NPDshCol1A1 and GL26) and human glioma cells
592 (MSP-12, SJGBM2) were maintained at 37 °C with 5% CO₂ and their respective media as described
593 before⁴¹⁻⁴⁴. Mouse NPA, NPD, NPAsCol1A1, NPDshCol1A1 neurospheres were derived from
594 genetically engineered tumor using the Sleeping Beauty (SB) transposase system as previously

595 described⁴¹⁻⁴⁴. Mouse GL26 glioma cells were generated by Sugiura K and obtained from the frozen
596 stock maintained by the National Cancer Institute (Bethesda, MD)²⁵. MSP-12 human glioma cell lines
597 were provided by Christine Brown, City of Hope, and SJGBM2 human glioma cells were provided by
598 Children's Oncology Group (COG) Repository, Health Science Center, Texas Tech University.

599 **Intracranial implantable syngeneic mouse gliomas:**

600 Glioma tumors were generated by stereotactic intracranial implantation into the mouse striatum of
601 3.0×10^4 mouse glioma cells (either, NPA, NPD or, GL26) in C57BL/6 mice, or human glioma cells in
602 immune-deficient NSG mice (SJGBM2) as described before^{42-44,68}. To test whether oncostream
603 tumor cells help move other cells throughout the tumor we generated a co-implantation glioma
604 model by intracranial implantation of highly malignant GL26-citrine cells with low aggressive human
605 MSP12 glioma cells at a ratio of 1:30 (1,000 GL26-citrine cells and 30,000 MSP12 cells) in immune-
606 deficient NSG mice. As controls, NSG mice were implanted with 30,000 MSP12 cells alone or 1,000
607 GL26-citrine cells alone as controls. Experiments were conducted according to the guidelines
608 approved by the Institutional Animal Care (IACUC) and Use Committee at the University of Michigan.
609 Stereotactic implantation was performed as previously described⁴².

610 **Genetically engineered mouse glioma models (GEMM)**

611 We used genetically engineered mouse glioma models for survival analysis and histopathological
612 analysis. Murine glioma tumors harboring different genetic drivers were generated using the
613 Sleeping Beauty (SB) transposon system as described before⁴¹⁻⁴⁴. Genetic modifications were
614 induced in postnatal day 1 (P01) male and female wild-type C57BL/6 mice (Jackson Laboratory),
615 according to IACUC regulations. shRNA targeting the COL1A1 gene was cloned as describe in detail
616 in Supplementary Methods.

617 **Analysis of oncostreams in human glioma tissue**

618 Oncostream presence was analyzed in unidentified H&E sections of paraformaldehyde-fixed
619 paraffin-embedded (PFPE) human glioma samples obtained from primary surgery from the
620 University of Michigan Medical School Hospital. To determine the presence of oncostreams in a
621 large cohort of human glioma tissues we used the biospecimens from "The Cancer Genome Atlas
622 Research Network" (TCGA) from the Genomic Data Commons Data Portal, National Cancer Institute,
623 NIH (<https://portal.gdc.cancer.gov>). We analyzed primary Glioblastoma multiforme (TCGA-GBM)
624 and Low-Grade Glioma (TCGA-LGG) databases. We selected cases that have available the Slide

625 Image and diagnostic Slides. The diagnostic slides are available for TCGA-GBM: 389 patients and
626 TCGA-LGG: 491 patients. The presence of oncostreams was scored on 100 TCGA-GBM Grade IV
627 tissue samples and 120 TCGA-LGG samples.

628 **Cell aspect ratio and alignment analysis in H&E tumor sections**

629 Images were obtained using bright-field microscopy of H&E stained paraffin sections (Olympus BX53
630 Upright Microscope). Tumors were imaged using 40X and 20X objectives. Images were processed
631 using the program ImageJ as indicated in detail in supplementary methods.

632 **Deep learning analysis for oncostreams detection on H&E staining of glioma tissue**

633 A fully convolutional neural network (fCNN) was trained in order to identify and segment
634 oncostreams in histologic images⁶⁹. We implemented a U-Net architecture to provide semantic
635 segmentation of glioma specimens using deep learning⁷⁰⁻⁷². Our oncostream dataset consisted of
636 images from mouse tissues and open-source images from The Cancer Genome Atlas (TCGA). A total
637 of 109 hematoxylin and eosin (H&E) stained histologic mouse images and 64 from TCGA were
638 reviewed and oncostreams were manually segmented by the study authors (AC, A.E.A and P.R.L.).
639 Images from both datasets were then augmented by randomly sampling regions within each image
640 to generate unique patches (~ 300 patches/image). The location and scale of each patch was
641 randomly chosen to allow for oncostream segmentation to be scale invariant. The analysis is
642 explained in further detail in Supplementary Methods.

643 **Immunohistochemistry on paraffin embedded brain tumors**

644 This protocol was performed as described before⁴² and as is detailed in Supplementary Methods.
645 Primary antibodies were diluted at the concentration indicated in Supplementary Table 8. Images
646 were obtained using bright-field microscopy from five independent biological replicates (Olympus
647 BX53 Upright Microscope). Ten different fields of each section were selected at random for study
648 to include heterogeneous tumor areas. For immunofluorescence on paraffin embedded sections
649 from brain tumors images were acquired with a laser scanning confocal microscope (LSM 880, Axio
650 Observer, Zeiss, Germany). Integrated density was determined for the analysis of Col1a1 expression
651 using Image J. For immunohistochemistry on vibratome brain tumor sections were left in 4%
652 paraformaldehyde fixation for 48 hours and then transferred to PBS 0.1% sodium azide for an
653 additional 24 hours at 4°C. A Leica VT100S vibratome was used to obtain 50 µm coronal brain
654 sections. The immunohistochemistry protocol was performed as previously described^{73,74}.

655 **Laser capture microdissection (LCM) of brain tumors**

656 Malignant glioma tumors were induced by intracranial implantation of dissociated NPA
657 neurospheres in C57BL/6 mice as described above. LCM approach to analyze differential mRNA
658 expression of intra-tumoral glioma heterogeneity was performed as described elsewhere⁷⁵.

659 **RNA-Sequencing and bioinformatics analysis**

660 RNA was isolated for laser microdissected tissues using the RNeasy Plus Micro Kit following the
661 manufacturer recommendations (Qiagen). Before library preparation, RNA was assessed for quality
662 using the TapeStation System (Agilent, Santa Clara, CA) using manufacturer's recommended
663 protocols. We obtained a RIN between 6 to 7 after laser microdissection of glioma tissue. A RIN of
664 6 was determined to be suitable for cDNA library preparation. 0.25 ng to 10 ng of total RNA was
665 used for cDNA library preparation using a kit suitable for RNA isolation at pico-molar concentrations
666 (MARTer Stranded Total RNA-Seq Kit v2 - Pico Input Mammalian) following manufacturer
667 recommended protocol (Clontech/Takara Bio #635005). Sequencing was performed by the UM DNA
668 Sequencing Core, using the Illumina Hi-Seq platform and Bioinformatic analysis were executed by
669 the UM Bioinformatics Core. Differentially expressed genes of all tumors were used for gene
670 ontology (GO), Pathways analysis and genes analysis using iPathwayGuide (Advaita Corporation
671 2021). Network analysis of the DE genes were achieved using Cytoscape and Reactome App.
672 Network was clustered by Reactome Functional Interaction (FI). Analysis of the expression of
673 COL1A1 in normal tissue and in human gliomas were performed using the dataset of TCGA-GBM
674 and TCGA-LGG from Gliovis (<http://gliovis.bioinfo.cnio.es>)⁴⁶.

675 **Tumor explant brain slice culture glioma model and time-lapse confocal imaging**

676 For the analysis of glioma dynamics, we generated tumors by intracranial implantation of 3×10^4
677 NPA neurospheres which were used to carry out a 3D explant slice culture glioma model. C57BL6
678 mice were used for the dynamic analyses of the tumor core and B6.129(Cg)-
679 Gt(ROSA)26Sortm4(ACTB-tdTomato,-EGFP)Luo/J- transgenic mice (Jackson laboratory, STOCK
680 007676) were used for invasion analysis. Mice were euthanized at 19 days' post-implantation for
681 NPA tumors and 31 days' post-implantation for NPashCOL1A1 tumors. Brains were removed,
682 dissected, and embedded in a 4% agarose solution and kept on ice for 5 minutes. Then, brains were
683 submerged in ice-cold and oxygenated media (DMEM High-Glucose without phenol red, Gibco™,
684 USA) and sectioned in a Leica VT100S vibratome (Leica, Buffalo Grove, IL) set to 300 μm in the z-

685 direction. All steps were performed under sterile conditions in a BSL2 laminar flow hood. Brain
686 tumor sections were transferred to laminin-coated Millicel Cell Culture Insert (PICMORG50,
687 Millipore Sigma, USA). Tumor slices were maintained in D-MEM F-12 media supplemented with 25%
688 FBS, Penicillin-Streptomycin 10.000 U/ML at 37 °C with a 5% CO₂ atmosphere for 24 hours. After 24
689 hours' media was replaced with DMEM-F12 media supplemented with B27 2%, N2 1%, Normocin
690 0.2 %, Penicillin-Streptomycin 10.000 U/ML and growth factors EGF and FGF 40 ng/ml. For time-
691 lapse imaging slices were placed in an incubator chamber of a single photon laser scanning confocal
692 microscope model LSM 880 (Carl Zeiss, Jena, Germany) at 37 °C with a 5% CO₂. Images were
693 obtained every ten minutes for 100-300 cycles. Following movie acquisition, sections were fixed in
694 4% paraformaldehyde (PFA) for 2 days. Fixed sections were embedded in 2% agarose for H&E and
695 immunohistochemistry analysis. Sections were processed and embedded in paraffin at the
696 University of Michigan Microscopy & Image Analysis Core Facility using a Leica ASP 300 paraffin
697 tissue processor/Tissue-Tek paraffin tissue embedding station (Leica, Buffalo Grove IL). Tumor
698 explants were used for collagenase treatment. Sections were then treated for 48 hours with
699 collagenase (C2399, MilliporeSigma, USA) at a concentration of 5, 10, or 15 units/ml or vehicle
700 control. Following treatment, sections were fixed in 4% paraformaldehyde (PFA) for 2 days.

701

702 **Cranial window implantation and two photon intravital live imaging *in vivo*:**

703 A craniotomy and cranial window implantation were performed following previously described
704 protocols by us and others^{25,76,77}. The protocol was conducted according to the guidelines approved
705 by the Institutional Animal Care (IACUC) and Use Committee at the University of Michigan. Briefly,
706 mice were anesthetized and placed in a stereotactic frame. A craniotomy of 3x3 mm size was made
707 over the right hemisphere in between bregma and lambda. 5x10⁴ GFP⁺ NPA glioma cells were
708 intracranially implanted at 0.8mm deep in the center of the craniotomy into the brain cortex of
709 B6.129(Cg)-Gt(ROSA)26Sortm4(ACTB-tdTomato-EGFP)Luo/J mice. The cranial window was created
710 with round microscope cover glass, and a metal head bar was positioned on the skull posterior to
711 the cranial window. One week post tumor cells injection and cranial window implantation, intravital
712 live imaging was performed using a two-photon microscope (Bruker Technology) with a 20X water
713 immersion objective (Olympus, NA 1.0) for 8-12 hours. The detailed methodology is available in
714 Supplementary Methods.

715

716

717 **Mathematical analysis of tumor cell movement**

718 To determine the movement of cells in different areas of the tumor we performed localized
719 statistical analysis in different zones of the tumor. We selected localized areas based on the
720 organization of cells in clusters, group of cells moving together with similar distribution. Raw data
721 of 4 movies from the tumor core and 4 movies from the tumor border were analyzed for 293 cycles
722 (core) and 186 cycles (border) for a frame rate of $\Delta t = 10$ min between image acquisition. To track
723 cell motion, we used the software Fiji with the plugin TrackMate⁷⁸. Analysis was performed as
724 indicated in detail in Supplementary Methods.

725 **Classification of glioma migration patterns**

726 To classify the collective cellular motion behavior of the three types of patterns called flock, stream,
727 and swarm illustrated in Supplementary Figure S10F we used as criteria the orientation of each cell
728 described by its unique angle velocity denoted θ_i . More precisely, we transformed the Angle
729 Velocity Distribution graph into a histogram where we examined the distribution of all the values
730 θ_i . A schematic representation of these distributions is depicted in Figure 4G. Considering a data-
731 set θ_n $n=1\dots N$ of orientations where N is the total number of cells, $\theta_n \in [0, 2\pi]$ is the direction of the
732 cell n . We tested three types of distributions p to describe the dataset and gave a likelihood in each
733 case as described in Supplementary Methods. **The Akaike Weight (AW) indicates which pattern has**
734 **the highest likelihood in each experimental situation⁷⁹.**

735 **Statistical Analysis**

736 All in vivo experiments were performed using independent biological replicates, as indicated in the
737 text and figures for each experiment. Data are shown as the mean \pm SEM. Any difference was
738 considered statistically significant when $p < 0.05$. In experiments that included one variable, the
739 one-way ANOVA test was used. In experiments with two independent variables, the two-way
740 ANOVA test was employed. A posterior Tukey's multiple comparisons test was used for mean
741 comparisons. Student's t-test was used to compare unpaired data from two samples. Survival data
742 were entered into Kaplan-Meier survival curves plots, and statistical analysis was performed using
743 the Mantel log-rank test. Median survival is expressed as MS. Significance was determined if $p < 0.05$.
744 All analyses were conducted using GraphPad Prism (version 8.0.0) or SAS (2021 SAS Institute, Cary,
745 NC). Each statistical test used is indicated within the figure legends.

746

747 **Data availability:** All data associated with this study are in the paper and/or the Supplementary
748 Information. RNA-Seq data was deposited NCBI's Gene Expression Omnibus (GEO) with identifiers
749 GSE188970. Further information and requests for resources and reagents should be directed to and
750 will be fulfilled by the corresponding authors P.R. Lowenstein.

751
752 **Code Availability:** The analysis of oncostreams in mouse and human glioma tissue was performed
753 using U-Net architecture to provide semantic segmentation of specimens using deep learning.
754 Public GitHub repository for the project code can be found at
755 <https://github.com/MLNeurosurg/DeepStreams>.

756 Analysis of glioma cells dynamics was performed using the Julia Programming Language. Link for this
757 project Script and their dependencies can be found at public GitHub repository
758 https://github.com/smotsch/analysis_glioma.

759

760 REFERENCES

- 761
762 1 Parsons, D. W. *et al.* An integrated genomic analysis of human glioblastoma multiforme. *Science*
763 (*New York, N.Y.*) **321**, 1807-1812, doi:10.1126/science.1164382 (2008).
764 2 Louis, D. N. *et al.* The 2007 WHO Classification of Tumours of the Central Nervous System. *Acta*
765 *Neuropathologica* **114**, 97-109, doi:10.1007/s00401-007-0243-4 (2007).
766 3 Ceccarelli, M. *et al.* Molecular Profiling Reveals Biologically Discrete Subsets and Pathways of
767 Progression in Diffuse Glioma. *Cell* **164**, 550-563, doi:10.1016/j.cell.2015.12.028 (2016).
768 4 Verhaak, R. G. *et al.* Integrated genomic analysis identifies clinically relevant subtypes of
769 glioblastoma characterized by abnormalities in PDGFRA, IDH1, EGFR, and NF1. *Cancer Cell* **17**, 98-
770 110, doi:10.1016/j.ccr.2009.12.020 (2010).
771 5 Sottoriva, A. *et al.* Intratumor heterogeneity in human glioblastoma reflects cancer evolutionary
772 dynamics. *Proceedings of the National Academy of Sciences of the United States of America* **110**,
773 4009-4014, doi:10.1073/pnas.1219747110 (2013).
774 6 Brennan, C. W. *et al.* The somatic genomic landscape of glioblastoma. *Cell* **155**, 462-477,
775 doi:10.1016/j.cell.2013.09.034 (2013).
776 7 Nicholson, J. G. & Fine, H. A. Diffuse Glioma Heterogeneity and Its Therapeutic Implications. *Cancer*
777 *discovery* **11**, 575-590, doi:10.1158/2159-8290.Cd-20-1474 (2021).
778 8 Puchalski, R. B. *et al.* An anatomic transcriptional atlas of human glioblastoma. *Science (New York,*
779 *N.Y.)* **360**, 660-663, doi:10.1126/science.aaf2666 (2018).
780 9 Wang, Q. *et al.* Tumor Evolution of Glioma-Intrinsic Gene Expression Subtypes Associates with
781 Immunological Changes in the Microenvironment. *Cancer Cell* **32**, 42-56.e46,
782 doi:10.1016/j.ccell.2017.06.003 (2017).
783 10 Patel, A. P. *et al.* Single-cell RNA-seq highlights intratumoral heterogeneity in primary glioblastoma.
784 *Science (New York, N.Y.)* **344**, 1396-1401, doi:10.1126/science.1254257 (2014).
785 11 Bergmann, N. *et al.* The Intratumoral Heterogeneity Reflects the Intertumoral Subtypes of
786 Glioblastoma Multiforme: A Regional Immunohistochemistry Analysis. *Front Oncol* **10**, 494,
787 doi:10.3389/fonc.2020.00494 (2020).
788 12 Garofano, L. *et al.* Pathway-based classification of glioblastoma uncovers a mitochondrial subtype
789 with therapeutic vulnerabilities. *Nat Cancer* **2**, 141-156, doi:10.1038/s43018-020-00159-4 (2021).
790 13 Kim, Y. *et al.* Perspective of mesenchymal transformation in glioblastoma. *Acta Neuropathol*
791 *Commun* **9**, 50, doi:10.1186/s40478-021-01151-4 (2021).
792 14 Hara, T. *et al.* Interactions between cancer cells and immune cells drive transitions to
793 mesenchymal-like states in glioblastoma. *Cancer Cell* **39**, 779-792.e711,
794 doi:10.1016/j.ccell.2021.05.002 (2021).

- 795 15 Neftel, C. *et al.* An Integrative Model of Cellular States, Plasticity, and Genetics for Glioblastoma.
796 *Cell* **178**, 835-849.e821, doi:10.1016/j.cell.2019.06.024 (2019).
- 797 16 Majc, B. *et al.* Epithelial-to-mesenchymal transition as the driver of changing carcinoma and
798 glioblastoma microenvironment. *Biochim Biophys Acta Mol Cell Res* **1867**, 118782,
799 doi:10.1016/j.bbamcr.2020.118782 (2020).
- 800 17 Azam, Z., To, S. T. & Tannous, B. A. Mesenchymal Transformation: The Rosetta Stone of
801 Glioblastoma Pathogenesis and Therapy Resistance. *Adv Sci (Weinh)* **7**, 2002015,
802 doi:10.1002/advs.202002015 (2020).
- 803 18 Behnan, J., Finocchiaro, G. & Hanna, G. The landscape of the mesenchymal signature in brain
804 tumours. *Brain* **142**, 847-866, doi:10.1093/brain/awz044 (2019).
- 805 19 Yang, J. *et al.* Guidelines and definitions for research on epithelial-mesenchymal transition. *Nat Rev*
806 *Mol Cell Biol* **21**, 341-352, doi:10.1038/s41580-020-0237-9 (2020).
- 807 20 Williams, E. D., Gao, D., Redfern, A. & Thompson, E. W. Controversies around epithelial-
808 mesenchymal plasticity in cancer metastasis. *Nat Rev Cancer* **19**, 716-732, doi:10.1038/s41568-019-
809 0213-x (2019).
- 810 21 Carro, M. S. *et al.* The transcriptional network for mesenchymal transformation of brain tumours.
811 *Nature* **463**, 318-325, doi:10.1038/nature08712 (2010).
- 812 22 Cheng, W. Y., Kandel, J. J., Yamashiro, D. J., Canoll, P. & Anastassiou, D. A multi-cancer
813 mesenchymal transition gene expression signature is associated with prolonged time to recurrence
814 in glioblastoma. *PLoS One* **7**, e34705, doi:10.1371/journal.pone.0034705 (2012).
- 815 23 Ray, A., Morford, R. K., Ghaderi, N., Odde, D. J. & Provenzano, P. P. Dynamics of 3D carcinoma cell
816 invasion into aligned collagen. *Integr Biol (Camb)* **10**, 100-112, doi:10.1039/c7ib00152e (2018).
- 817 24 Pickup, M. W., Mouw, J. K. & Weaver, V. M. The extracellular matrix modulates the hallmarks of
818 cancer. *EMBO Rep* **15**, 1243-1253, doi:10.15252/embr.201439246 (2014).
- 819 25 Baker, G. J. *et al.* Mechanisms of glioma formation: iterative perivascular glioma growth and
820 invasion leads to tumor progression, VEGF-independent vascularization, and resistance to
821 antiangiogenic therapy. *Neoplasia* **16**, 543-561, doi:10.1016/j.neo.2014.06.003 (2014).
- 822 26 Deisboeck, T. S. & Couzin, I. D. Collective behavior in cancer cell populations. *Bioessays* **31**, 190-197,
823 doi:10.1002/bies.200800084 (2009).
- 824 27 Friedl, P., Locker, J., Sahai, E. & Segall, J. E. Classifying collective cancer cell invasion. *Nat Cell Biol*
825 **14**, 777-783, doi:10.1038/ncb2548 (2012).
- 826 28 Friedl, P. & Mayor, R. Tuning Collective Cell Migration by Cell-Cell Junction Regulation. *Cold Spring*
827 *Harb Perspect Biol* **9**, doi:10.1101/cshperspect.a029199 (2017).
- 828 29 Méhes, E. & Vicsek, T. Collective motion of cells: from experiments to models. *Integr Biol (Camb)* **6**,
829 831-854, doi:10.1039/c4ib00115j (2014).
- 830 30 Rørth, P. Fellow travellers: emergent properties of collective cell migration. *EMBO Rep* **13**, 984-991,
831 doi:10.1038/embo.2012.149 (2012).
- 832 31 Friedl, P. & Gilmour, D. Collective cell migration in morphogenesis, regeneration and cancer. *Nat*
833 *Rev Mol Cell Biol* **10**, 445-457, doi:10.1038/nrm2720 (2009).
- 834 32 Scarpa, E. & Mayor, R. Collective cell migration in development. *J Cell Biol* **212**, 143-155,
835 doi:10.1083/jcb.201508047 (2016).
- 836 33 Theveneau, E. & Mayor, R. Neural crest delamination and migration: from epithelium-to-
837 mesenchyme transition to collective cell migration. *Dev Biol* **366**, 34-54,
838 doi:10.1016/j.ydbio.2011.12.041 (2012).
- 839 34 Alieva, M. *et al.* Intravital imaging of glioma border morphology reveals distinctive cellular
840 dynamics and contribution to tumor cell invasion. *Scientific reports* **9**, 2054, doi:10.1038/s41598-
841 019-38625-4 (2019).
- 842 35 Haeger, A., Krause, M., Wolf, K. & Friedl, P. Cell jamming: collective invasion of mesenchymal tumor
843 cells imposed by tissue confinement. *Biochim Biophys Acta* **1840**, 2386-2395,
844 doi:10.1016/j.bbagen.2014.03.020 (2014).

- 845 36 Brett, E. A., Sauter, M. A., Machens, H. G. & Duscher, D. Tumor-associated collagen signatures:
846 pushing tumor boundaries. *Cancer Metab* **8**, 14, doi:10.1186/s40170-020-00221-w (2020).
- 847 37 Mammoto, T. *et al.* Role of collagen matrix in tumor angiogenesis and glioblastoma multiforme
848 progression. *Am J Pathol* **183**, 1293-1305, doi:10.1016/j.ajpath.2013.06.026 (2013).
- 849 38 Fang, M., Yuan, J., Peng, C. & Li, Y. Collagen as a double-edged sword in tumor progression. *Tumour*
850 *Biol* **35**, 2871-2882, doi:10.1007/s13277-013-1511-7 (2014).
- 851 39 Payne, L. S. & Huang, P. H. The pathobiology of collagens in glioma. *Mol Cancer Res* **11**, 1129-1140,
852 doi:10.1158/1541-7786.MCR-13-0236 (2013).
- 853 40 Pointer, K. B. *et al.* Association of collagen architecture with glioblastoma patient survival. *J*
854 *Neurosurg* **126**, 1812-1821, doi:10.3171/2016.6.JNS152797 (2017).
- 855 41 Calinescu, A. A. *et al.* Transposon mediated integration of plasmid DNA into the subventricular zone
856 of neonatal mice to generate novel models of glioblastoma. *Journal of visualized experiments* :
857 *JoVE*, doi:10.3791/52443 (2015).
- 858 42 Comba, A. *et al.* Fyn tyrosine kinase, a downstream target of receptor tyrosine kinases, modulates
859 anti-glioma immune responses. *Neuro-oncology* **22**, 806-818 (2020).
- 860 43 Koschmann, C. *et al.* ATRX loss promotes tumor growth and impairs nonhomologous end joining
861 DNA repair in glioma. *Sci Transl Med* **8**, 328ra328, doi:10.1126/scitranslmed.aac8228 (2016).
- 862 44 Núñez, F. J. *et al.* IDH1-R132H acts as a tumor suppressor in glioma via epigenetic up-regulation of
863 the DNA damage response. **11**, eaaq1427, doi:10.1126/scitranslmed.aaq1427 %J Science
864 Translational Medicine (2019).
- 865 45 Brat, D. J. *et al.* Comprehensive, Integrative Genomic Analysis of Diffuse Lower-Grade Gliomas. *N*
866 *Engl J Med* **372**, 2481-2498, doi:10.1056/NEJMoa1402121 (2015).
- 867 46 Bowman, R. L., Wang, Q., Carro, A., Verhaak, R. G. & Squatrito, M. GlioVis data portal for
868 visualization and analysis of brain tumor expression datasets. *Neuro-oncology* **19**, 139-141,
869 doi:10.1093/neuonc/now247 (2017).
- 870 47 Jamous, S., Comba, A., Lowenstein, P. R. & Motsch, S. Self-organization in brain tumors: How cell
871 morphology and cell density influence glioma pattern formation. *PLoS computational biology* **16**,
872 e1007611 (2020).
- 873 48 Bialek, W. *et al.* Statistical mechanics for natural flocks of birds. *Proceedings of the National*
874 *Academy of Sciences of the United States of America* **109**, 4786-4791,
875 doi:10.1073/pnas.1118633109 (2012).
- 876 49 Szabó, A. & Mayor, R. Mechanisms of Neural Crest Migration. *Annu Rev Genet* **52**, 43-63,
877 doi:10.1146/annurev-genet-120417-031559 (2018).
- 878 50 Staneva, R. *et al.* Cancer cells in the tumor core exhibit spatially coordinated migration patterns.
879 *Journal of cell science* **132**, doi:10.1242/jcs.220277 (2019).
- 880 51 Egeblad, M., Rasch, M. G. & Weaver, V. M. Dynamic interplay between the collagen scaffold and
881 tumor evolution. *Curr Opin Cell Biol* **22**, 697-706, doi:10.1016/j.ceb.2010.08.015 (2010).
- 882 52 Provenzano, P. P. *et al.* Collagen reorganization at the tumor-stromal interface facilitates local
883 invasion. *BMC Med* **4**, 38, doi:10.1186/1741-7015-4-38 (2006).
- 884 53 Shintani, Y., Hollingsworth, M. A., Wheelock, M. J. & Johnson, K. R. Collagen I promotes metastasis
885 in pancreatic cancer by activating c-Jun NH(2)-terminal kinase 1 and up-regulating N-cadherin
886 expression. *Cancer research* **66**, 11745-11753, doi:10.1158/0008-5472.CAN-06-2322 (2006).
- 887 54 Kim, H., Watkinson, J., Varadan, V. & Anastassiou, D. Multi-cancer computational analysis reveals
888 invasion-associated variant of desmoplastic reaction involving INHBA, THBS2 and COL11A1. *BMC*
889 *Med Genomics* **3**, 51, doi:10.1186/1755-8794-3-51 (2010).
- 890 55 Glioma through the looking GLASS: molecular evolution of diffuse gliomas and the Glioma
891 Longitudinal Analysis Consortium. *Neuro-oncology* **20**, 873-884, doi:10.1093/neuonc/now020
892 (2018).
- 893 56 Behnan, J. *et al.* Differential propagation of stroma and cancer stem cells dictates tumorigenesis
894 and multipotency. *Oncogene* **36**, 570-584, doi:10.1038/onc.2016.230 (2017).

- 895 57 Dolor, A. & Szoka, F. C., Jr. Digesting a Path Forward: The Utility of Collagenase Tumor Treatment
896 for Improved Drug Delivery. *Mol Pharm* **15**, 2069-2083, doi:10.1021/acs.molpharmaceut.8b00319
897 (2018).
- 898 58 Diop-Frimpong, B., Chauhan, V. P., Krane, S., Boucher, Y. & Jain, R. K. Losartan inhibits collagen I
899 synthesis and improves the distribution and efficacy of nanotherapeutics in tumors. *Proceedings of*
900 *the National Academy of Sciences of the United States of America* **108**, 2909-2914,
901 doi:10.1073/pnas.1018892108 (2011).
- 902 59 Kumar, S., Henning-Knechtel, A., Magzoub, M. & Hamilton, A. D. Peptidomimetic-Based
903 Multidomain Targeting Offers Critical Evaluation of A β Structure and Toxic Function. *J Am Chem Soc*
904 **140**, 6562-6574, doi:10.1021/jacs.7b13401 (2018).
- 905 60 Kato, M., Hattori, Y., Kubo, M. & Maitani, Y. Collagenase-1 injection improved tumor distribution
906 and gene expression of cationic lipoplex. *Int J Pharm* **423**, 428-434,
907 doi:10.1016/j.ijpharm.2011.12.015 (2012).
- 908 61 Lee, S. *et al.* Extracellular matrix remodeling in vivo for enhancing tumor-targeting efficiency of
909 nanoparticle drug carriers using the pulsed high intensity focused ultrasound. *J Control Release* **263**,
910 68-78, doi:10.1016/j.jconrel.2017.02.035 (2017).
- 911 62 Hambardzumyan, D., Gutmann, D. H. & Kettenmann, H. The role of microglia and macrophages in
912 glioma maintenance and progression. *Nat Neurosci* **19**, 20-27, doi:10.1038/nn.4185 (2016).
- 913 63 Gritsenko, P. G. & Friedl, P. Adaptive adhesion systems mediate glioma cell invasion in complex
914 environments. *Journal of cell science* **131**, doi:10.1242/jcs.216382 (2018).
- 915 64 Gritsenko, P. G. *et al.* p120-catenin-dependent collective brain infiltration by glioma cell networks.
916 *Nat Cell Biol* **22**, 97-107, doi:10.1038/s41556-019-0443-x (2020).
- 917 65 Peglion, F., Llense, F. & Etienne-Manneville, S. Adherens junction treadmill during collective
918 migration. *Nat Cell Biol* **16**, 639-651, doi:10.1038/ncb2985 (2014).
- 919 66 Lim, D. A. & Alvarez-Buylla, A. The Adult Ventricular-Subventricular Zone (V-SVZ) and Olfactory Bulb
920 (OB) Neurogenesis. *Cold Spring Harb Perspect Biol* **8**, doi:10.1101/cshperspect.a018820 (2016).
- 921 67 Waclaw, B. *et al.* A spatial model predicts that dispersal and cell turnover limit intratumour
922 heterogeneity. *Nature* **525**, 261-264, doi:10.1038/nature14971 (2015).
- 923 68 Kamran, N. *et al.* Current state and future prospects of immunotherapy for glioma. *Immunotherapy*
924 **10**, 317-339, doi:10.2217/imt-2017-0122 (2018).
- 925 69 Shelhamer, E., Long, J. & Darrell, T. Fully Convolutional Networks for Semantic Segmentation. *IEEE*
926 *Trans Pattern Anal Mach Intell* **39**, 640-651, doi:10.1109/tpami.2016.2572683 (2017).
- 927 70 Sharma, M., Pachori, R. & Acharya, U. R. Adam: a method for stochastic optimization. *Pattern*
928 *Recognit. Lett* **94**, 172-179 (2017).
- 929 71 Hollon, T. C. *et al.* Near real-time intraoperative brain tumor diagnosis using stimulated Raman
930 histology and deep neural networks. *Nat Med* **26**, 52-58, doi:10.1038/s41591-019-0715-9 (2020).
- 931 72 Ronneberger, O., Fischer, P. & Brox, T. U-Net: Convolutional Networks for Biomedical Image
932 Segmentation. *Springer International Publishing* 234-241 (2015).
- 933 73 Wilson, T. J., Zamlar, D. B., Doherty, R., Castro, M. G. & Lowenstein, P. R. Reversibility of glioma
934 stem cells' phenotypes explains their complex in vitro and in vivo behavior: Discovery of a novel
935 neurosphere-specific enzyme, cGMP-dependent protein kinase 1, using the genomic landscape of
936 human glioma stem cells as a discovery tool. *Oncotarget* **7**, 63020-63041,
937 doi:10.18632/oncotarget.11589 (2016).
- 938 74 Yadav, V. N. *et al.* CXCR4 increases in-vivo glioma perivascular invasion, and reduces radiation
939 induced apoptosis: A genetic knockdown study. *Oncotarget* **7**, 83701-83719,
940 doi:10.18632/oncotarget.13295 (2016).
- 941 75 Comba, A. *et al.* Laser Capture Microdissection of Glioma Subregions for Spatial and Molecular
942 Characterization of Intratumoral Heterogeneity, Oncostreams, and Invasion. *JoVE (Journal of*
943 *Visualized Experiments)*, e60939 (2020).
- 944 76 Huber, D. *et al.* Multiple dynamic representations in the motor cortex during sensorimotor
945 learning. *Nature* **484**, 473-478, doi:10.1038/nature11039 (2012).

- 946 77 Chen, Z., Ross, J. L. & Hambardzumyan, D. Intravital 2-photon imaging reveals distinct morphology
947 and infiltrative properties of glioblastoma-associated macrophages. *Proceedings of the National*
948 *Academy of Sciences of the United States of America* **116**, 14254-14259,
949 doi:10.1073/pnas.1902366116 (2019).
- 950 78 Tinevez, J. Y. *et al.* TrackMate: An open and extensible platform for single-particle tracking.
951 *Methods* **115**, 80-90, doi:10.1016/j.ymeth.2016.09.016 (2017).
- 952 79 Kenneth P. Burnham, D. R. A. *Model selection and multimodel inference: A practical information-*
953 *theoretic approach*. 2 edn, (Springer, 2002).

954

955 **ACKNOWLEDGMENTS**

956 We thank all members of our laboratory for advice and comments on this work. This work was
957 supported by National Institutes of Health, National Institute of Neurological Disorders and Stroke
958 (NIH/NINDS) grants: R37-NS094804, R01-NS105556, R21-NS107894, R21-NS091555; R01-NS074387
959 to M.G.C.; National Institute of Neurological Disorders and Stroke (NIH/NINDS) grants: R01-
960 NS076991, R01-NS096756, R01-NS082311 to P.R.L.; National Institute of Biomedical Imaging and
961 Bioengineering (NIH/NIBI): R01-EB022563; National Cancer Institute (NIH/NCI) U01CA224160; Rogel
962 Cancer Center at The University of Michigan G023089 to M.G.C. Ian's Friends Foundation grant
963 G024230, Leah's Happy Hearts Foundation grant G013908, Pediatric Brain Tumor Foundation grant
964 G023387 and ChadTough Foundation grant G023419 to P.R.L. RNA Biomedicine grant: F046166 to
965 M.G.C. Health and Human Services, National Institutes of Health, UL1 TR002240 to Michigan
966 Institute for Clinical and Health Research (MICHR), Postdoctoral Translational Scholars Program
967 (PTSP), Project F049768 to A.C.

968

969 **AUTHORS INFORMATION**

970 **Affiliations:**

971

972 **Dept. of Neurosurgery, University of Michigan Medical School, Ann Arbor, 48109, MI, USA**

973 Andrea Comba, Syed M. Faisal, Patrick J. Dunn, Todd C. Hollon, Wajd N. Al-Holou, Maria Luisa Varela,
974 Daniel B. Zamler, Anna E. Argento, Phillip E. Kish, Maria G Castro, Pedro R. Lowenstein

975

976 **Dept. of Cell and Developmental Biology, University of Michigan Medical School, Ann Arbor,**
977 **48109 MI, USA**

978 Andrea Comba, Syed M. Faisal, Patrick J. Dunn, Maria Luisa Varela, Daniel B. Zamler, Anna E.
979 Argento, Maria G Castro, Pedro R. Lowenstein

980

981 **Rogel Cancer Center, University of Michigan medical School, Ann Arbor, 48109, MI, USA**

982 Andrea Comba, Syed M. Faisal, Patrick J. Dunn, Maria Luisa Varela, Daniel B. Zamler, Maria G Castro,
983 Pedro R. Lowenstein

984

985 **School of Mathematical and Statistical Sciences, Arizona State University, Tempe, AZ, USA**

986 Sebastien Motsch

987

988 **Ophthalmology & Visual Science, University of Michigan Medical School, Ann Arbor, 48109 MI,**
989 **USA**

990 Phillip E. Kish, Alon Kahana

991
992
993
994
995
996
997
998
999
1000
1001
1002
1003
1004
1005
1006
1007
1008
1009
1010
1011
1012
1013
1014
1015
1016
1017
1018
1019
1020
1021
1022
1023
1024
1025
1026
1027
1028
1029
1030
1031

Dept. of Pathology, University of Michigan Medical School, Ann Arbor, MI 48109, USA

Celina G. Kleer

**Kresge Hearing Research Institute, Department of Otolaryngology-Head & Neck Surgery,
University of Michigan medical School, Ann Arbor, MI 48109, USA**

Gunnar L Quass, Pierre F. Apostolides

**Dept. of Molecular & Integrative Physiology, University of Michigan medical School, Ann Arbor,
MI 48109, USA**

Pierre F. Apostolides

**Departments of Hematology & Hematopoietic Cell Transplantation and Immuno-Oncology, City
of Hope, Duarte, CA, USA**

Christine E. Brown

Contributions: Conception and design: A. Comba, M.G. Castro, P. R. Lowenstein. Development of methodology: A. Comba, M.S. Faisal, P. J. Dunn, A. E. Argento, T. Hollon, W.N. Al-Holou, M.L. Varela, D.B. Zamler, S. Motsch, P. R. Lowenstein. Acquisition of data, analysis, and interpretation: A. Comba, M.S. Faisal, P. J. Dunn, A. E. Argento, T. Hollon, M.L. Varela, D.B. Zamler, M.G. Castro, S. Motsch, P. R. Lowenstein. Human histopathology analysis and identification of oncostreams: A. Comba, C. Kleer, A. E. Argento, P. R. Lowenstein. Laser microdissection protocol: A. Comba, P. R. Lowenstein, P. E. Kish, Alon Kahana. Development and establishment of intravital imaging using multiphoton microscopy: Comba, M.S. Faisal, P. R. Lowenstein, G. L. Quass, P. F. Apostolides. Development and experimental assistance with human glioma cell lines. development and assistance: C.E. Brown. Manuscript writing: A. Comba, S. Motsch, P. R. Lowenstein. Administrative, technical, or material support (i.e., reporting or organizing data, constructing databases): A. Comba, P. R. Lowenstein. Study supervision: M. G. Castro and P. R. Lowenstein. All authors reviewed the final version of the manuscript.

Corresponding author:

Correspondence to Pedro R. Lowenstein

ETHICS DECLARATIONS

Competing interests: All authors of this paper declare no potential conflicts of interest.

1032 **Figure Legends**

1033

1034 **Fig. 1. Oncostreams are multicellular fascicles present in mouse and human gliomas**

1035 **A)** Representative 5 μm H&E microtome sections from gliomas showing that fascicles of spindle-like
1036 glioma cells (oncostreams, outlined by the dotted line) are present in a GEMM of gliomas NPA
1037 (NRAS/shATRx/shp53) and the GL26 intracranial implantable model of glioma. Scale bars: 50 μm . **B)**
1038 Representative H&E microtome sections of human glioma and human xenografts showing the
1039 presence of oncostreams. Scale bar: 20 μm . **C-D)** Histograms showing the cellular shape analysis
1040 (aspect ratio) **(C)** and angle orientation (alignment) for the corresponding images **(D)** shows areas of
1041 oncostreams (OS) formed by elongated and aligned cells and areas with no oncostreams (No-OS) as
1042 rounded and not-aligned cells. **E-G)** Immunostaining show that tumor cells, mesenchymal cells
1043 (ACTA2+), microglia/macrophages (IBA1+ and CD68+), are aligned within, the main orientation axis
1044 of oncostreams. Scale bar: 20 μm . Bar graphs show the quantification of ACTA+, n=3 **(E)**, IBA1+, n=5
1045 **(F)** and CD68+, n=5 **(G)** cells within oncostreams areas in NPA tumors. 6-13 areas of oncostreams per
1046 tumor section per animal were imaged. Error bars represent \pm SEM; unpaired t-test analysis,
1047 *p<0.05, **p<0.001. **H)** Angle orientation shows the alignment of ACTA+, IBA1+ and CD68+ cells
1048 within oncostreams for the corresponding images.

1049

1050 **Fig. 2. Oncostreams density positively correlates with tumor aggressiveness in GEMM of gliomas.**

1051 **A)** Genetic makeup of NPA and NPAI tumors. **B)** Kaplan–Meier survival curves of NPA and NPAI mouse
1052 gliomas show that animals bearing IDH1-R132H mutant tumors (NPAI) have prolonged median
1053 survival (MS): **NPA** (MS: 86 days; n: 18) versus **NPAI** (MS: 213 days; n:12). Log-rank (Mantel-Cox) test;
1054 ****p<0.0001. **C-D)** Deep learning method for oncostream detection in H&E stained mouse glioma
1055 sections: **C)** Representative images of oncostreams manually segmented on H&E stained sections of
1056 NPA gliomas and NPAI tumors. The output of our trained model for each image is shown below
1057 (probability heat maps), for tissues containing oncostreams (NPA), and without oncostreams (NPAI),
1058 scale bar = 100 μm . **D)** 10-14 random fields per tumor section per animal were imaged, n=9 NPA and
1059 n=12 NPAI, and quantified using deep learning analysis. Error bars represent \pm SEM; unpaired t-test
1060 analysis, *p<0.05. **E)** Angle histogram plots show aligned cells in NPA tumors vs non-aligned cells in
1061 NPAI tumors for the representative images showed in figure.

1062

1063 **Fig. 3. The density of oncostreams positively correlates with tumor aggressiveness in human**

1064 **gliomas. A)** TCGA tumors were analyzed from different grade: GBM-Grade IV (100 tumors). LGG-
1065 Grade III (70 tumors) and LGG-Grade II (50 tumors). Pie charts show percentage of tumors displaying
1066 oncostreams in relation to tumor grade. Oncostreams are present in 47% of GBM grade IV tumors,
1067 8.6 % of LGG grade III, and are absent from LGG grade II. **B)** Manual identification of oncostreams in
1068 H&E images are shown for human gliomas with WHO grades IV, III, II from TCGA. **C)** Deep learning
1069 analysis for human gliomas. Our algorithm was able to detect oncostreams in grade IV and III gliomas
1070 but not in grade II gliomas. **D)** Angle histogram plots show the alignment of cells in H&E histology
1071 sections of Grade IV and Grade III gliomas' oncostreams and random alignment in grade II glioma
1072 sections lacking oncostreams. Angle histogram correspond to the representative images. **E-F)**
1073 Immuno-fluorescence staining of SOX2+ tumor cells (green), glial fibrillary acidic protein (GFAP+)
1074 cells (red), and microglia/macrophage (IBA1+) cells (red) in high-grade human glioblastoma (GBM)
1075 (WHO Grade IV), IDH-WT **(E)** and in low-grade glioma (LGG) (WHO Grade III), IDH-mutant **(F)**,
1076 showing oncostreams heterogeneity and cellular alignment in human high-grade gliomas but not in
1077 low grade gliomas. Scale bars: 50 μm .

1078 **Fig. 4. Oncostreams are defined by a unique gene expression signature related to mesenchymal**
1079 **transformation and migration. A)** Schematic representation of spatial transcriptomic analysis of
1080 glioma oncostreams using Laser Capture Microdissection (LCM). Glioma tumors were generated by
1081 intracranial implantation of NPA tumor cells in C57BL6 mice (a). Oncostream areas (red outline) were
1082 identified and dissected from surrounding glioma tissue (black outline) in mouse glioma samples
1083 using a LCM microscope (b-c). **B)** A volcano plot displays differentially expressed (DE) genes from
1084 oncostream vs no-oncostream areas. DE genes were selected based on a fold change of ≥ 1.5 and a
1085 q-value (false discovery rate (FDR) corrected p-value) of ≤ 0.05 . Upregulated genes (red dots) and
1086 downregulated genes (green dots) are shown. Relevant genes related to mesenchymal migration are
1087 labeled on the graph. **C)** Heat map illustrates gene expression patterns for oncostream vs no-
1088 oncostream areas in NPA glioma tumors (n=3 biological replicates/group). Differentially upregulated
1089 genes (16) are represented in red and downregulated genes (n=27) are represented in green (q-
1090 value ≤ 0.05 and fold change $\geq \pm 1.5$). **D)** Functional enrichment analysis of overrepresented GO
1091 terms (biological processes) obtained when comparing oncostream vs no-oncostream DE genes. p-
1092 value corrected for multiple comparisons using the FDR method. Cutoff FDR <0.05 . Blue:
1093 Downregulated GOs. Red: upregulated GOs. **E)** Bar graphs show DE genes annotated to the most
1094 relevant enriched GOs biological process: “Positive regulation of cell motility”, “Regulation of cell
1095 migration” and “Collagen metabolic process.”

1096
1097 **Fig. 5. COL1A1 is a central hub in oncostream organization and glioma malignancy. A)** Network
1098 analysis of the DE genes comparing oncostreams versus no-oncostreams DE genes. Genes with a
1099 higher degree of connectivity are highlighted with larger nodes. Clusters of nodes with the same
1100 color illustrate modules of highly interacting of genes in the network. **B)** Immunofluorescence
1101 analysis of COL1A1 expression in GEMM of glioma tissues comparing NPA (IDH1-WT) vs NPAI
1102 (IDH1mut). Representative confocal images display COL1A1 expression in green (Alexa 488) and
1103 nuclei in blue (DAPI). Scale bar: 50 μm . **C)** Bar graphs represent COL1A1 quantification in terms of
1104 fluorescence integrated density. NPA n=5 and NPAI n=6 animals for each experimental condition
1105 were used for the analysis. Ten fields of each tumor section were selected at random. Error bars
1106 represent \pm SEM. t-test, **p <0.01 . **D)** Immunofluorescence analysis of COL1A1 expression in human
1107 GBM and LGG tumors. COL1A1 expression in green (Alexa 488) and nuclei in blue (DAPI). Scale bar:
1108 50 μm . **E)** Bar graphs represent COL1A1 quantification as fluorescence integrated density. 5 (LGG)
1109 and 8 (GBM) tumor samples were used for the analysis. Ten fields of each tumor section were
1110 selected at random. Error bars represent \pm SEM. t-test, **p <0.01 . **F-G)** GEMM of glioma with COL1A1
1111 inhibition. **F)** Kaplan–Meier survival curve comparing NPA (MS: 68 days; n: 14) vs NPashCOL1A1 (MS:
1112 123 days; n: 28) **G)** Kaplan–Meier survival curve comparing NPD (MS: 74 days; n=15) versus
1113 NPDshCOL1A1 (MS: 98 days; n=17). Log-rank (Mantel-Cox) test. **** p <0.0001 , **p <0.0126 . **H)**
1114 Immunofluorescence analysis of COL1A1 expression in GEMM of glioma controls (NPA and NPD) and
1115 Col1A1 downregulation (NPashCOL1A1 and NPDshCOL1A1). Representative confocal images of
1116 COL1A1 expression in green (Alexa 488) and nuclei in blue (DAPI). Scale bar: 50 μm . **I)** Bar graphs
1117 represent COL1A1 quantification in terms of fluorescence integrated density. 5-7 tumor samples for
1118 each experimental condition were used for the analysis. Ten fields of each tumor section were
1119 selected at random. Error bars represent \pm SEM. t-test, **p <0.01 . **J)** Representative images of the
1120 histopathological identification of oncostreams in H&E tissue sections comparing the COL1A1
1121 knockdown tumors with their respective controls. Scale bars: 50 μm . **K)** Quantitative analysis of
1122 oncostream areas using deep learning analysis. 4-12 tumor samples for each experimental condition
1123 were used for the analysis. Error bars represent \pm SEM; unpaired t-test analysis, *p <0.05 .

1124 **Fig. 6. Knockdown of COL1A1 within glioma cells modifies the tumor microenvironment**
1125 Immunohistochemical analysis (**A, C** and **E**) of GEMM of glioma controls (**NPA** and **NPD**) and COL1A1
1126 downregulation (**NPAshCOL1A1** and **NPDshCOL1A1**). **A**) Representative images of PCNA expression.
1127 Scale bar: 20 μm . **B**) Bar graphs represent the quantification of PCNA+ cells numbers (cells/mm²)
1128 using QuPath positive cell detection. Error bars represent \pm SEM, (NPA: n=8, NPAshCOL1A1: n=5,
1129 NPD: n=8, NPDshCOL1A1: n=4), t-test, * $p < 0.05$. **C**) Representative images of CD68 expression. Scale
1130 bar: 20 μm . **D**) Bar graphs represent CD68+ cell quantification (cells/mm²) using QuPath positive cell
1131 detection. Error bars represent \pm SEM, (NPA: n=8, NPAshCOL1A1: n=5, NPD: n=6, NPDshCOL1A1:
1132 n=4), t-test, * $p < 0.05$, ns: no significant. **E**) Representative images of CD31 expression. Scale bar: 20
1133 μm . **F**) Bar graphs represent CD31+ cells quantification (cells/mm²) using QuPath positive cells
1134 detection. Error bars represent \pm SEM, (NPA: n=8, NPAshCOL1A1: n=5, NPD: n=6, NPDshCOL1A1:
1135 n=4), t-test, ** $p < 0.01$, * $p < 0.05$. **G**) Immunofluorescence analysis of GEMM of glioma controls (**NPA**
1136 and **NPD**) and COL1A1 downregulation (**NPAshCOL1A1** and **NPDshCOL1A1**). Representative images
1137 of ACTA2 expression in red (Alexa 555) and nuclei in blue (DAPI). Scale bar: 50 μm . **H**) Bar graphs
1138 represent ACTA2 quantification in terms of fluorescence integrated density. Error bars represent
1139 \pm SEM, (NPA: n=6, NPAshCOL1A1: n=5, NPD: n=4, NPDshCOL1A1: n=3), t-test, ** $p < 0.001$, ns: no
1140 significant.

1141
1142 **Fig. 7. Collective dynamics of oncostreams increase cell spreading within the tumor core. A)**
1143 Experimental setup: NPA-GFP glioma cells were intracranially implanted in C57BL6 mice. Explant
1144 slice cultures of growing tumors were used for confocal time-lapse imaging of the tumor core. **B)**
1145 Single representative time-lapse confocal image of glioma cells within the tumor core (Movie #1). **C)**
1146 Tracking analysis of individual cell paths performed using the Track-Mate plugin from Image-J. **D)**
1147 Preferred directions of cells within three zones (A-C) superimposed onto a representative time lapse-
1148 image. **E)** Speed distribution and mean speed ($\mu\text{m}/\text{hr}$) in Zones A, B and C. **F)** Distribution of angle
1149 velocity for each zone. The Angle Velocity of each cell is denoted ϑ . The plot shows the proportion
1150 of cells moving in angle direction ϑ for each zone. **G-H)** Classification of collective motion patterns:
1151 *stream*, *flock* or *swarm*. The distribution is *uni-modal* for a flock (only one peak) and *bi-modal* for a
1152 stream (two peaks = 2 preferred angle velocity). For a *swarm*, the distribution is *flat* (no preferred
1153 angle velocity). In **G)** Angle Velocity was transformed to a histogram; these data were then used to
1154 calculate the likelihood that a particular distribution of velocity angles corresponds to either a
1155 *stream*, *flock*, or *swarm*. The results are given in **H)** for each zone. The frequency distribution of the
1156 data (shown in black) uses a *non-parametric* estimation (kernel density estimator). We tested three
1157 types of distributions, p , to describe the data-sets and give a likelihood for each case. The best fit
1158 was then determined by the Akaike weight (AW). **I)** Co-implantation of highly malignant GL26-citrine
1159 cells (green) and human MSP-12 glioma stem cells (ratio 1:30), and MSP-12 cells alone (control – left
1160 image). Immunohistochemistry of human nuclei (black) denote MSP-12 cells. Arrows show the
1161 distribution of MSP-12 cells within the brain or the tumor. Scale bar: 100 μm . **J)** Quantification of the
1162 distance of MSP-12 from the site of implantation. n=3 for control and n=5 for co-implantation (MSP-
1163 12+GL26). Error bars \pm SEM; t-test, * $p < 0.05$. **K)** Immunofluorescence images of human-nestin (red)
1164 labeling MSP-12 cells, and GL26-citrine cells. Note that MSP-12 cells have a multipolar morphological
1165 structure when alone, but a bipolar, elongated structure when aligned to GL26-citrine cells. Scale
1166 bar: 47.62 μm . **L)** Angle histogram plots quantify the alignment of MSP-12 within oncostreams, and
1167 the random alignment of MSP-12 cells when implanted alone (with dashed overlays of the other
1168 condition's alignment).

1169 **Fig. 8. Collective invasion of COL1A1 enriched oncostreams contributes to malignant glioma**
1170 **behavior. A)** Schematic representation of the experimental setup and location of imaging and
1171 quantification of tumor borders using td/mtTomato mice (Movie #5). **B)** Representative time-lapse
1172 scanning confocal image of glioma cells at the tumor border. This image was taken from border
1173 movie #1 and shows the subdivision into different zones. **C)** Preferred direction of cells within
1174 different zones superimposed onto a representative time lapse-image. **D)** Histogram of speed
1175 distribution and mean speed ($\mu\text{m}/\text{h}$) of Zones A, B, C and D. **E)** Angle Velocity distribution analysis
1176 (ϑ) performed by zones. Plot shows overall direction and magnitude of cell movement. **F)** Likelihood
1177 analysis of the dynamic patterns at the tumor border. Graph of density estimation ρ flock (red), ρ
1178 stream (yellow) and ρ swarm (blue). The estimation of the black line (data) uses a *non-parametric*
1179 estimation. AW: 0 or AW:1. **G)** Immunofluorescence analysis of GFP expression in GEMM of glioma
1180 controls (NPA), and NPashCOL1A1. Representative confocal images of the tumor borders. GFP
1181 expression is shown in green (Alexa 488) and nuclei in blue (DAPI). Dotted lines show tumor borders.
1182 Stars show tumor cell invasion patterns. Scale bar: 50 μm . **H)** The analysis of tumor borders was
1183 determined using the Allen-Cahn equation. Images were split into two values (-1 and +1)
1184 representing the inside and outside of the tumor to analyze the sinuosity of the borders. Illustration
1185 of the sinuosity of a curve: it is defined as the ratio between the length of the curve L and the
1186 distance between the two extreme points. The sinuosity is close to 1 for a straight line. **I)** Sinuosity
1187 of the border for all experiments. 4-10 images of each tumor border were obtained. NPA: n=6 and
1188 NPashCOL1A1: n=5 tumors for each experimental condition were used for the analysis. We detected
1189 a decrease of the sinuosity in COL1A1 knockdown tumors. t-test unequal variance, *p=0.0297.

1190
1191 **Fig. 9. Intravital two-photon imaging reveals the collective patterns of glioma dynamics**
1192 **oncostream dynamics *in vivo*.**

1193 **A)** Representative picture of the cranial window showing metallic head-bar positioned on the skull
1194 posterior to the cranial window and affixed using dental cement to stabilize the imaging plane and
1195 minimize motion artifacts during the time-lapse imaging. **B)** Single representative time-lapse two-
1196 photon image of glioma cells within the tumor core *in vivo* (Movie #13). **C)** Tracking analysis of
1197 individual cell paths of the *in vivo* time-lapse. **D)** Speed distribution and mean speed in $\mu\text{m}/\text{hr}$
1198 considering as a single zone named Zone A. **E)** Angle Velocity distribution for the *in vivo* time-lapse.
1199 The Angle Velocity of each cell is denoted θ . Plot shows overall direction and magnitude of cell
1200 movement in Zone A. **F)** Likelihood analysis of the dynamic patterns in *in vivo* intravital imaging.
1201 Graph of density estimation ρ flock (red), ρ stream (yellow) and ρ swarm (blue). The estimation of
1202 the black line (data) uses a *non-parametric* estimation. AW: 0 or AW:1. **G)** Single representative time-
1203 lapse two-photon image of glioma cells invasion in the brain cortex *in vivo* (Movie #14). **H)** Individual
1204 cell paths trajectories of the *in vivo* time-lapse experiment. **I)** Preferred direction of cells within
1205 three zones (A-C) superimposed onto a representative *in vivo* time-lapse image determined by
1206 likelihood analysis. **J)** Speed distribution and mean speed ($\mu\text{m}/\text{hr}$) in Zone A, Zone B, and Zone
1207 C. **K)** Angle Velocity distribution for the invasion *in vivo* time-lapse for each zone. The Angle Velocity
1208 of each cell is denoted θ . The plot shows the proportion of cells moving in the angle direction θ for
1209 each zone. **L)** Likelihood analysis of the dynamic patterns in *Movie #14* by intravital imaging. Graph
1210 of density estimation ρ flock (red), ρ stream (yellow) and ρ swarm (blue). The estimation of the black
1211 line (data) uses a *non-parametric* estimation. AW: 0 or AW:1.

1212
1213

1214 **Fig. 10. Oncostreams are COL1A1-rich multicellular dynamic mesenchymal structures that regulate**
1215 **glioma invasion and malignancy.** Summary representation of mesenchymal dynamic fascicles
1216 (oncostreams) present in high grade gliomas. Our study reveals that oncostreams display directional
1217 collective motility patterns including streams and flocks. Non-directional collective motion (swarms)
1218 are represented by round cells that move do not have a preferred direction of motion. Directional
1219 dynamic patterns function as tumoral highways to facilitate the intra-tumoral spread of cells and
1220 participate in local invasion of normal brain. Oncostreams are areas of mesenchymal transformation
1221 defined by a molecular signature enriched in COL1A1. COL1A1 knockdown disrupts oncostream
1222 organization, decreases intratumoral heterogeneity and significantly increases animal survival. Our
1223 study reveals that oncostreams are anatomically and molecularly distinctive, are areas of
1224 mesenchymal transformation organized through interactions with the COL1A1 matrix, move by
1225 collective motion, and regulate glioma growth and invasion.

1226

1227

1228 **SUPPLEMENTARY INFORMATION**

1229 **Supplementary Material and Methods**

1230 **Supplementary Figures**

1231 **Supplementary Tables**

1232 **Supplementary Videos**

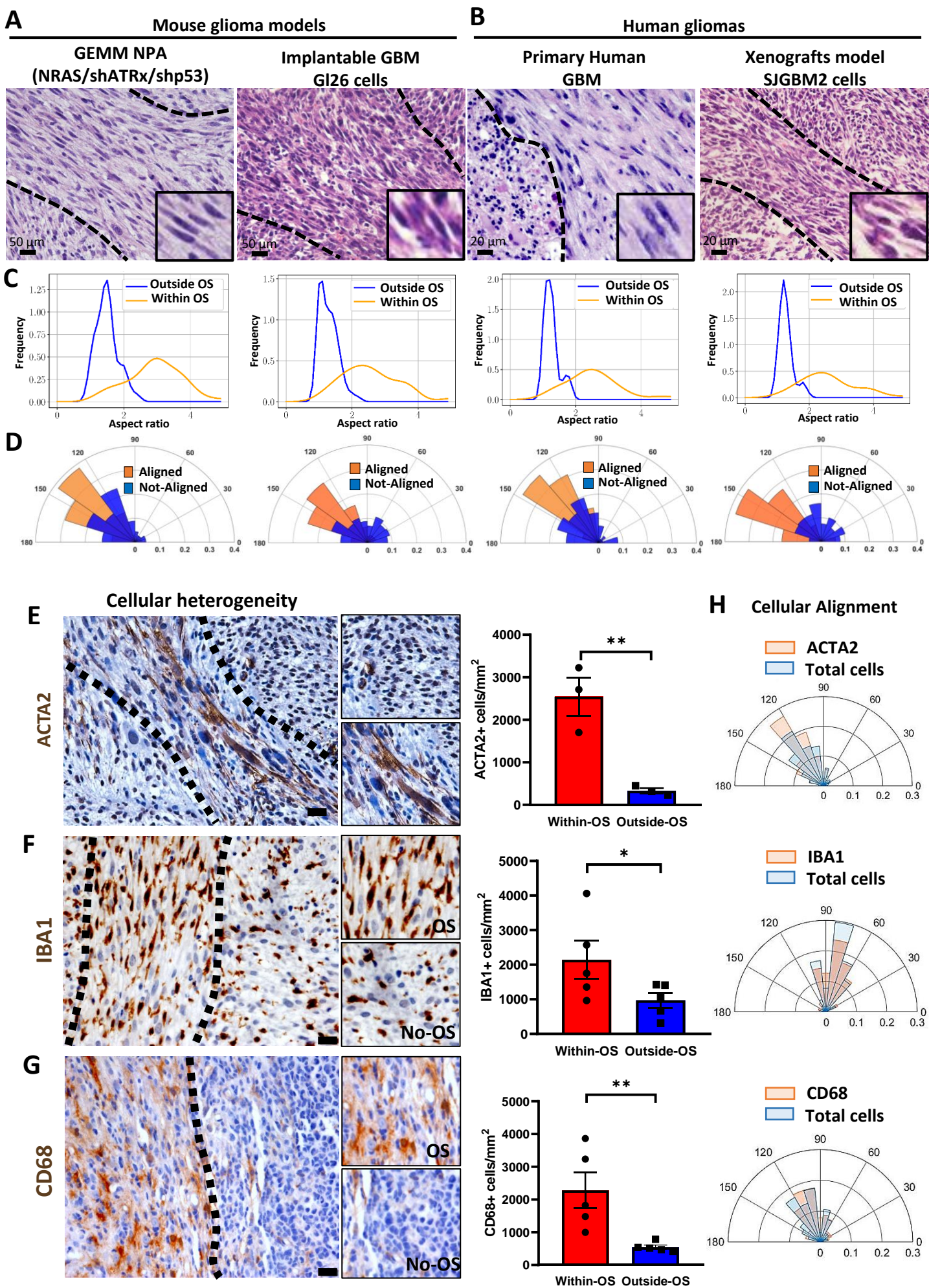


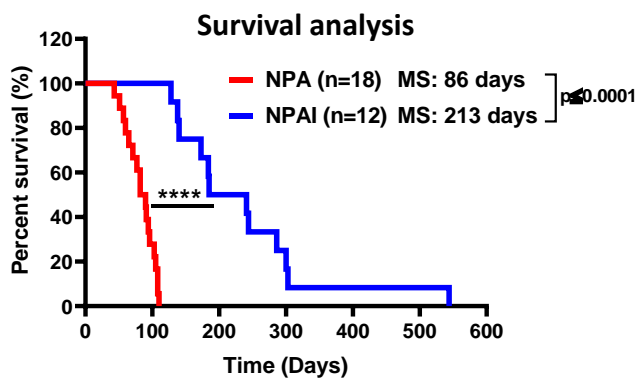
Fig. 2

A

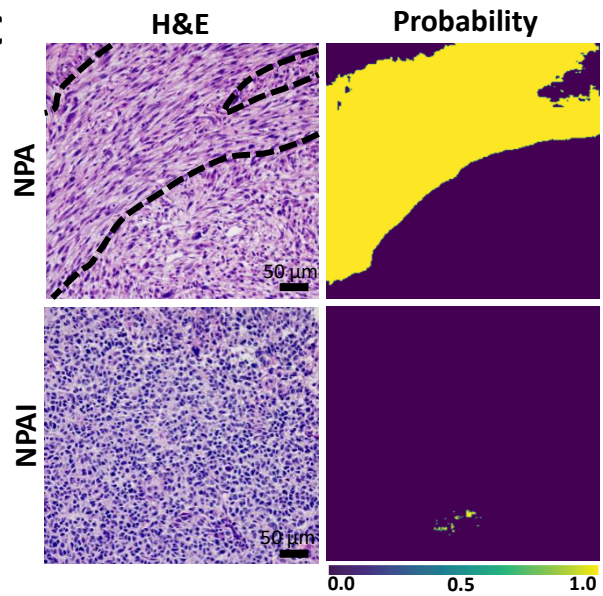
GEMM of glioma

Tumor	Genetic modifications
NPA	NRAS-GV12/shP53-GFP/shATRX-GFP
NPAI	NRAS-GV12/shP53-GFP/shATRX-GFP/IDH1-R132H

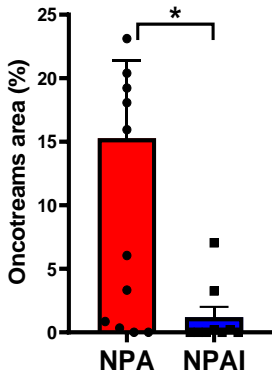
B



C



D



E

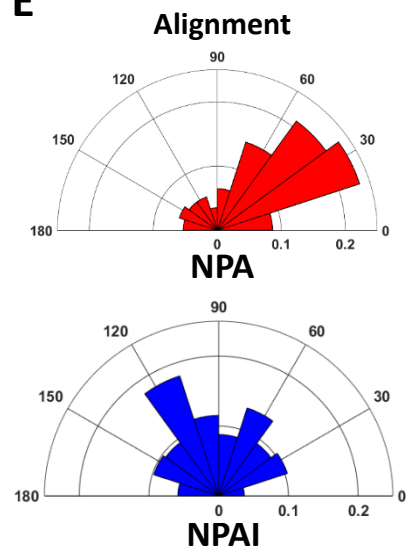


Fig. 3

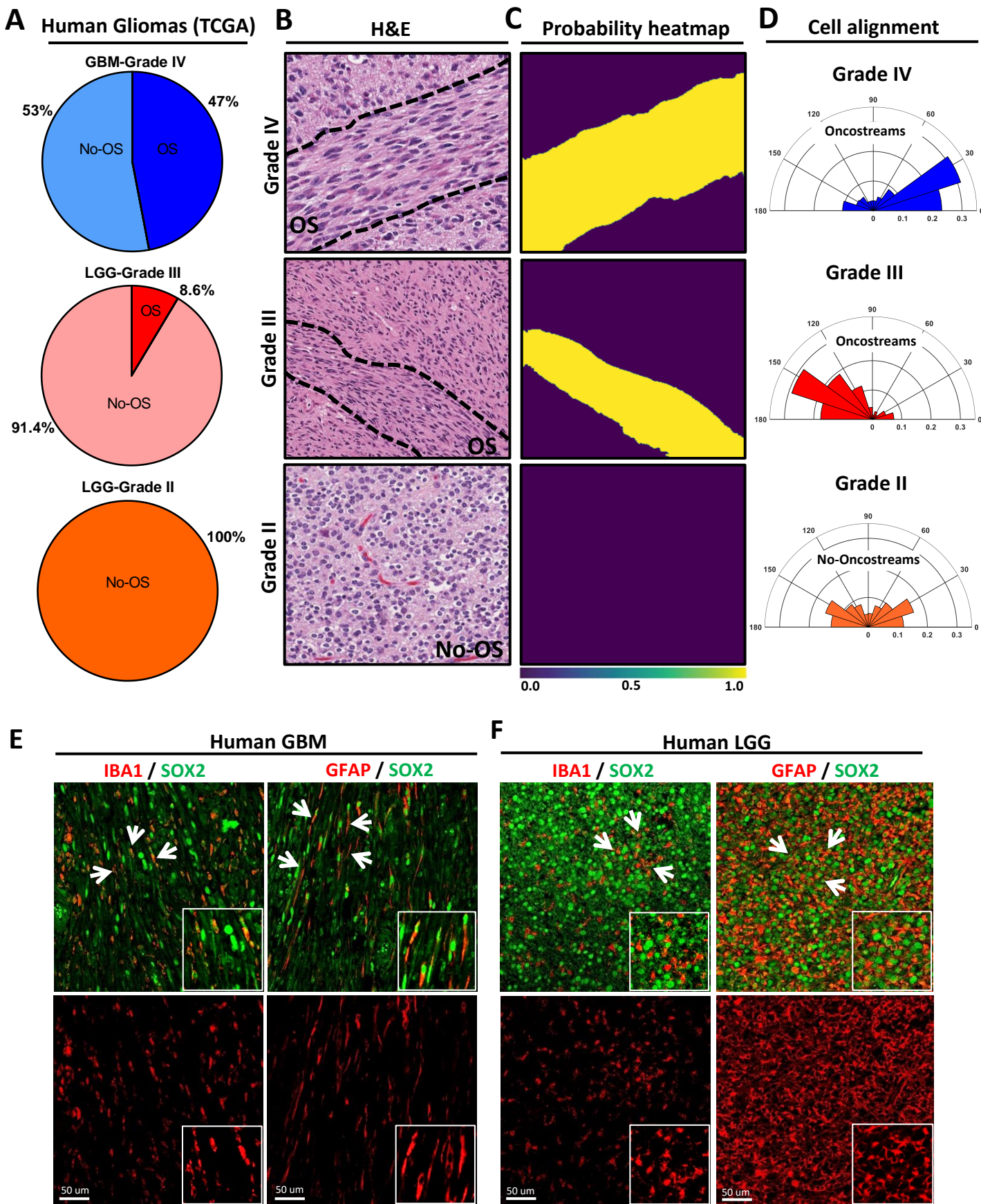


Fig. 4

